Design and Continuous (Re)Processing of Thermally Resilient Poly(Styrene-co-Maleic Maleate)-Based Covalent Adaptable Networks

Aitor Hernández, Tim Maiheu, Eric Drockenmuller, Damien Montarnal, Johan Winne, Filip Du Prez

Design and Continuous (Re)Processing of Thermally Resilient Poly(Styrene-*co*-Maleic Maleate)-based Covalent Adaptable Networks

*Aitor Hernández,[a] Tim Maiheu,[a] Eric Drockenmuller,[b] Damien Montarnal,[c] Johan M. Winne[a] and Filip E. Du Prez[a]**

[a]*Polymer Chemistry Research Group, Centre of Macromolecular Chemistry, and Laboratory for Organic Synthesis, Department of Organic and Macromolecular Chemistry, Faculty of Sciences, Ghent University, Krijgslaan 281 S4, Ghent B-9000, Belgium.*

[b]*Université Claude Bernard Lyon 1, CNRS, Ingénierie des Matériaux Polymères, UMR 5223, 69100 Villeurbanne, France*

[c]*Université Claude Bernard Lyon 1, CPE Lyon, CNRS, Catalyse, Chimie, Polymères et Procédés, UMR 5265, 69100 Villeurbanne, France.*

* E-mail: Filip.DuPrez@UGent.be

KEYWORDS: Covalent Adaptable Network, dissociative covalent bond, recyclable thermoset, extrusion, injection molding.

ABSTRACT: Cyclic anhydrides, classical monomers for bulk synthetic materials, have recently gained attention in covalent adaptable networks (CANs). They undergo reversible ring-opening with polyols, forming dynamic monoester linkages. This inherent property makes cyclic anhydrides ideal for industrially relevant polymer matrices with CAN-like recycling and reprocessing capabilities. Our study presents a rational design for poly(styrene-*co*-maleic maleate) monoester (PS-MME)-based polymer networks, achieved by crosslinking commercially available poly(styrene-*co*-maleic anhydride) (PS-*co*-MA) with a series of diols. The network synthesis is not only feasible on a large scale and under solvent-free conditions, but also allows for the tailoring of the final crosslinking degree and properties by independently tuning the PS-*co*-MA maleic anhydride content, its chain length and/or the loading of crosslinker diols used. Previous limitations in thermal stability of MME-based CANs, stemming from remaining free carboxyl acids in mono-ester linkages, are circumvented through the dilution of reactive sites in an apolar matrix and switching to a cyclic anhydride ring embedded into the polymer backbone. This robust macromolecular architecture enhances the kinetics and thermodynamics of reversible mono-ester formation, resulting in PS-MMEs with exceptional thermal resilience. Even at temperatures exceeding 210°C, PS-MMEs exhibit fast crosslink exchange without compromising their rheological, mechanical, or thermal properties. This feature not only enables continuous (re)processing via extrusion and injection molding, but a chemical recycling study also demonstrates a solvent-assisted recovery of the pure starting polyol monomers and PS-*co*-MA linear polymers, facilitating their use in new polymer materials. In other words, this research paves the way for industrially applicable CANs by leveraging widely used bulk monomers and polymers.

Introduction

Traditionally, the selection of a polymer material for any given application is based on the distinctive properties that differentiate thermoplastics[1] from thermosets.[2] While the permanent network structure of the latter results in a more robust structural integrity for high demand applications,[3] it also comes with a reduced amenability to thermomechanical or chemical recycling (as thermoplastics offer).[4] In this context, covalent adaptable networks (CANs)[5,6] emerged industrially as an alternative option, capable of unifying the superior mechanical properties of thermosets and the (re)processability of thermoplastics because of their capability to flow when subjected to stimuli such as light, pH changes, ultrasonic waves or elevated temperatures.[7,8]

The defining characteristics of CANs originate from topological network rearrangements, either through associative mechanisms (in material science also referred to as vitrimers)[9–11] or through reversible decrosslinking as a result of reversible equilibria following a dissociative mechanism.[12–17] For a clearer understanding and optimization of the design and properties of temperature-triggered dissociative CANs, it is essential to appreciate the intricate synergy between the functionality of the constituent building blocks, the thermodynamic parameters controlling the lifetime (τ_{bond}) and mass balance of adduct and dissociated species, and on the other hand the resulting temperature dependence of the viscoelastic properties.[14] This relationship will ultimately determine the flow properties of the CAN at a particular temperature.[8,10] For example, networks featuring low functionality building blocks, ranging from small molecules to oligomers, could potentially result in a low-viscosity material, even when the dynamic bonds are only partially dissociated.[18,19] On the other hand, networks synthesized from

highly entangled polymer backbones display a rheological behavior that is constrained by the parent polymer precursor, in alignment with the Rouse model and the corresponding relaxation time (τ_R).[20–23] For such networks, a complete dissociation may not be achievable and the chain dynamics are thus expected to follow the so-called 'sticky Rouse model'.[24]

In all cases, the network connectivity and thermal responsivity would still be determined by the dynamic bond's thermodynamic nature, as the reaction enthalpies and entropies govern the dissociation equilibrium.[8,13] A high reaction enthalpy lowers the degree of dissociation, while the reaction entropy generally favors the decrosslinked state. Recently, many studies reported CANs that were synthesized from thermoplastic precursors based on commodity thermoplastics such as polyolefins,[9,25–27] poly(meth)acrylates,[16,28,29] or polystyrene (PS).[14,30–32] This strategy has been recognized to offer good opportunities to translate CANs into industrially relevant applications, as a small degree of reversible crosslinking could already improve the material's properties when compared to their non-crosslinked counterparts (*e.g.*, tensile strength, solvent, creep or stress cracking resistance), thus opening novel end user opportunities while retaining their (re)processability.

An attractive strategy to entropically favor the rate of bond dissociation is that of the neighboring group participation,[33] as has been demonstrated in materials based on phthalate monoesters (PMEs) for example.[19,34] Such CANs have relatively high activation energies but benefit from neighboring nucleophilic or acidic groups involved in covalent exchange reaction mechanisms, increasing the dissociation rate without lowering enthalpic barriers. Since their implementation in CANs, a large variety of dynamic chemistries that exploit an internally catalyzed ring closure mechanism has been developed.[17,18,35–37]

While targeting an industrially attractive protocol for the continuous reprocessing of PS-based CANs, the starting point of this study was the creation of dissociative CANs from poly(styrene-*co*-maleic anhydride) (PS-*co*-MA) copolymers that are widely used as compatibilizers for polymer blends.[38,39]

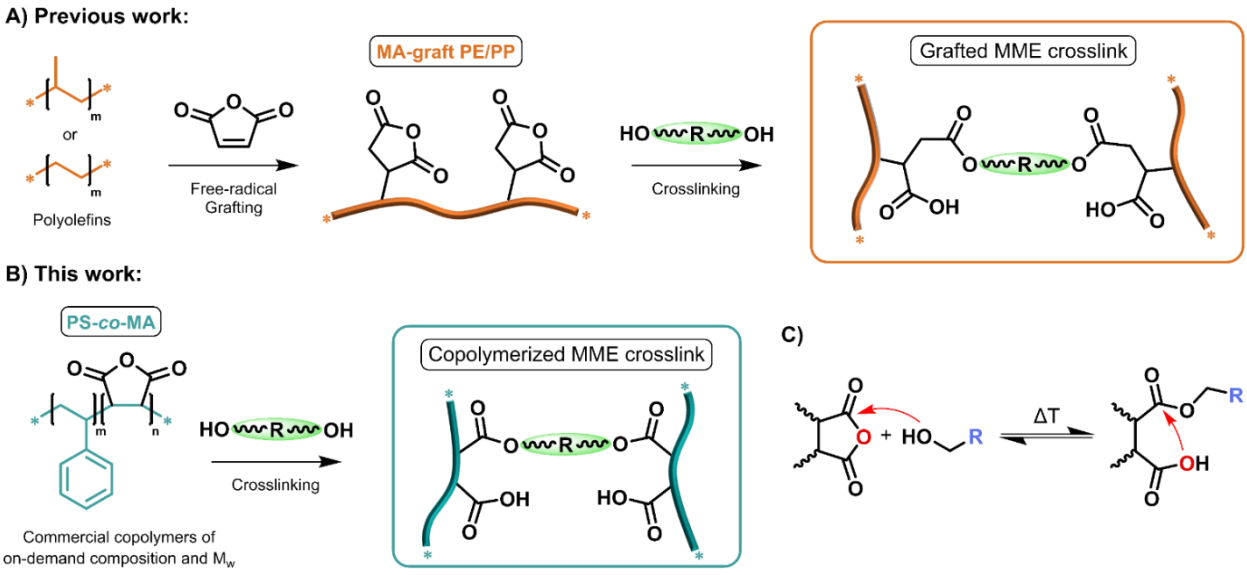

Scheme 1. A) Maleic anhydride radical-mediated grafting procedure used as a dynamic transesterification moiety,[25,41] synthetic handle[40,43] or grafted MA monoesters.[44,45] B) Schematic representation of the synthesis of PS-MMEs developed in this study, including copolymerized MA monoesters. C) Dissociative crosslink rearrangement mechanism involved in PS-MME CANs.

Maleic anhydride (MA) reactive units have already been used as synthetic handles[40] or grafted on thermoplastics to provide dynamic crosslinks. Terentjev and coworkers demonstrated in particular their combination with polyols to form transesterification-based CANs.[25,41] Also, direct copolymerization of styrene with MA has been explored very recently in the field of CANs by Ma and coworkers.[42] They applied the MA-units as a way to crosslink PS with an acetal containing diol to dominate the bond exchange in dual dynamic networks. As a straightforward alternative, herein we report a strategy for the synthesis of PS-based CANs

(further referred to as PS-MMEs) from two PS-*co*-MAs of high and low molecular weight and commercially available diols (**Scheme 1.B**), where the resulting *maleate monoester* (MME) crosslinks are able to reversibly dissociate into alcohols and cyclic anhydrides upon heating (**Scheme 1.C**).

From those reports, it remains unclear how copolymerized MA monoester structures compare with polymer materials in which MA has been grafted incorporated through radical-mediated reactions (**Scheme 1.A-B**).[44–46] Based on our experience with anhydride-containing precursors for the design of CANs,[19] we hypothesized that, in contrast to materials with grafted-MA pending groups, the MA-moieties inserted in the polymer backbone could have a positive impact on rheological properties and overcome thermal limitations. Indeed, it is well known that PMEs and MME-based materials undergo branching or crosslinking side reactions after exposure at temperatures above 180°C, which strongly impedes their (re)processing.[35,44–47] The present work will therefore focus on the crosslinking of two commercial and quasi-random PS-*co*-MA copolymers both above and below their critical entanglement molecular weight (M_c),[48,49] which are industrially obtained *via* starve-fed copolymerization involving constant comonomer feedings.[50,51] We compare upscalable PS-MME synthesis protocols with various functionalization ratios and molar masses, both in solution and bulk. Furthermore, we propose a comprehensive study of their viscoelastic and rheological properties.

Finally, we will show that the readily accessible PS-MMEs represent an inexpensive and easily processable class of dissociative CANs, with ideal chemistry and rheological profiles to allow for high resilience at service temperatures, easy reprocessing *via* extrusion or injection molding, and upcycling back to the parent polymers.

Experimental procedures

Synthesis of PS-MME CANs in solution. To a 250 mL Teflon® beaker immersed in an oil bath and equipped with a magnetic stirrer, 70 mL of tetrahydrofuran (THF) was added. Afterwards, 10 g of Xibond® 120 (**PS-*co*-MA$_{191k}$**), Xibond® 220 (**PS-*co*-MA$_{13k}$**) (**Scheme 2.A**) or polystyrene-*b*-poly(ethylene-*r*-butylene)-*b*-polystyrene-*g*-maleic anhydride 2 wt% (**SEBS-*g*-MA**) beads (**Scheme 2.A**) were slowly poured into the beaker while stirring. The beaker opening was then covered and heated to 60°C. Once the beads had completely dissolved, targeting specific stoichiometric ratios as stated in **Tables S2-S4** in Supporting Information, the specified amounts of Pripol™ 2033 (PP2033), 1,4-cyclohexanedimethanol (CHDM), β-amino alcohol (BA) or Priamine™ 1074 (PA1074) see **Scheme 2.A** were dissolved in 10 mL of THF and added to the beaker. Next, the mixture was covered again, the temperature was then set to 70°C and the solution was left to stir and concentrate overnight. Finally, the remaining solvent was removed by heating the mixture inside the beaker in an oven at 100°C for 1 h and then 4 h at 140°C (180°C overnight and under vacuum for network **H$_S$PA$_{100}$**, see the beginning of the results and discussion section for an overview of the systematic sample coding and **Table 1** for a detailed network composition summary). All PS-MME CANs were obtained as colorless, glassy transparent materials.

Synthesis of PS-MME CANs in bulk. The synthesis of PS-MME CANs in bulk indicated in **Table 1** was conducted using a twin rotor single batch internal mixer. To the chamber of the mixer, preheated to 180°C and set at 50 rpm, PS-*co*-MA$_{191k}$ or PS-*co*-MA$_{13k}$ beads (**Scheme 2.A**) were added according to **Tables S2-S4**. Once the torque and temperature had stabilized, the corresponding amount of PP2033 (**Scheme 2.A**) was added with a syringe by injecting the diol through the feeding hole straight into the chamber. Then, the mixing was allowed to proceed

until the torque and temperature stabilized (always below 210°C) (**Figure S1**). Lastly, the warm material was removed from the screws as a white solid. All PS-MMEs were then annealed under vacuum at 140°C for 2 h to afford colorless and transparent glassy materials.

Room temperature solubility tests. Solubility tests were conducted using sets of at least six discs of 2 to 3 mm thickness obtained using a 3 mm diameter puncher on the preheated single-pressed samples. The discs were then annealed at 140°C for two hours and slowly cooled down. The different samples were then immersed in 40 mL of acetone for 7 days in 40mL vials and the acetone was renewed on the 2nd, 4th and 6th day. The swollen discs were weighed on the 7th day, immediately after removing the non-swollen acetone from the discs by momentarily placing them on top of a paper towel. Then the samples were dried overnight under vacuum at 140°C. The swelling ratios and soluble fractions were calculated using equations *(1)* and *(2)*, where m_0, m_s, m_d are the initial, swollen state and dry masses of the respective samples and the soluble fractions were analyzed through ^{1}H-NMR (**Figure S16**).

$$Swelling\ Ratio\ (\%) = \frac{m_s - m_d}{m_d} \times 100 \qquad (1)$$

$$Soluble\ Fraction\ (\%) = \frac{m_0 - m_d}{m_0} \times 100 \qquad (2)$$

Solvent spillage resistance test. A comparison was conducted between the acetone spillage resistance on smooth surfaces of network $\mathbf{H_SPP_{10}}$ (**Table 1**) and a commercial polystyrene (M_w = 192 kg/mol). Disks with a 22 mm diameter and 0.1 mm thickness were prepared by compression molding the materials between two Teflon sheets placed between two smooth steel plates (500 kPa, 30 min, 180°C). Then, the films were cut using a preheated circular blade and vacuum-annealed at 140°C for 2 h, sandwiched between the previously used steel plates. The samples were then transferred over a smooth polypropylene surface on a bench protected from air drafts

at room temperature. Using a micro-pipette, a single drop of 50 μL was gently deposited on the surface of the films from a height of approximately 2 cm. The acetone was then left to permeate the samples at room temperature for 24 h. The integrity and transparency of the affected areas were visually evaluated by positioning the samples over a paper sheet containing printed *lorem ipsum* text in Calibri (body) font (size 8) to highlight potential defects such as surface cloudiness or crack formations.

Results and discussion

The synthesis of a series of PS-MME CANs from commercial PS-*co*-MA copolymers and diols (**Scheme 2.A**) has been carried out both in solution as well as in bulk (see experimental procedures and **Scheme 2.B**). The materials synthesized on this project were named following a systematic $\boldsymbol{A_BC_D}$ labeling code in which ***A*** stands for the polymer precursor used: '**L**-series' (from Low M_w) for PS-*co*-MA_{13k}, '**H**-series' (from High M_w) for PS-*co*-MA_{191k} and '**G**-series' (from Grafted) for the MA-grafted **SEBS-*g*-MA** terpolymer. ***B*** refers to the synthesis method: '**S**-series' for Solution and '**B**-series' for Bulk. ***C*** indicates the bifunctional crosslinker used: '**PP**' for Pripol™ 2033, '**CH**' for 1,4-cyclohexanedimethanol, '**BA**' for a 70/30 $mol_{\%}$ mixture of a β-amino alcohol and Pripol™ 2033 and '**PA**' for Priamine™ 1074) (**Schemes S1-S3**). Finally, ***D*** (*i.e.,* '**100'**, '**50**', '**25**' and '**10**' ending values) specifies the reacting nucleophile/MA $mol_{\%}$ ratio used in the synthesis of the materials.

A material composition reference appendix, including an acronym glossary, is provided at the start of the Supporting Information section to facilitate easy reference to material formulations and abbreviations found in the main manuscript. Yet, an overview of all PS-MME, composition, synthesis protocols and properties can also be found below in **Table 1**. As will be discussed in

following sections, high glass transition temperature (T_g) values (*i.e.,* av $T_g \geq 80$°C), high thermal stability and resilience, exceptional property retention upon recycling and improved solvent resistance were observed (*vide infra*). An in-depth study of the molecular structure and its possible relationship to mechanical and rheological properties was conducted.

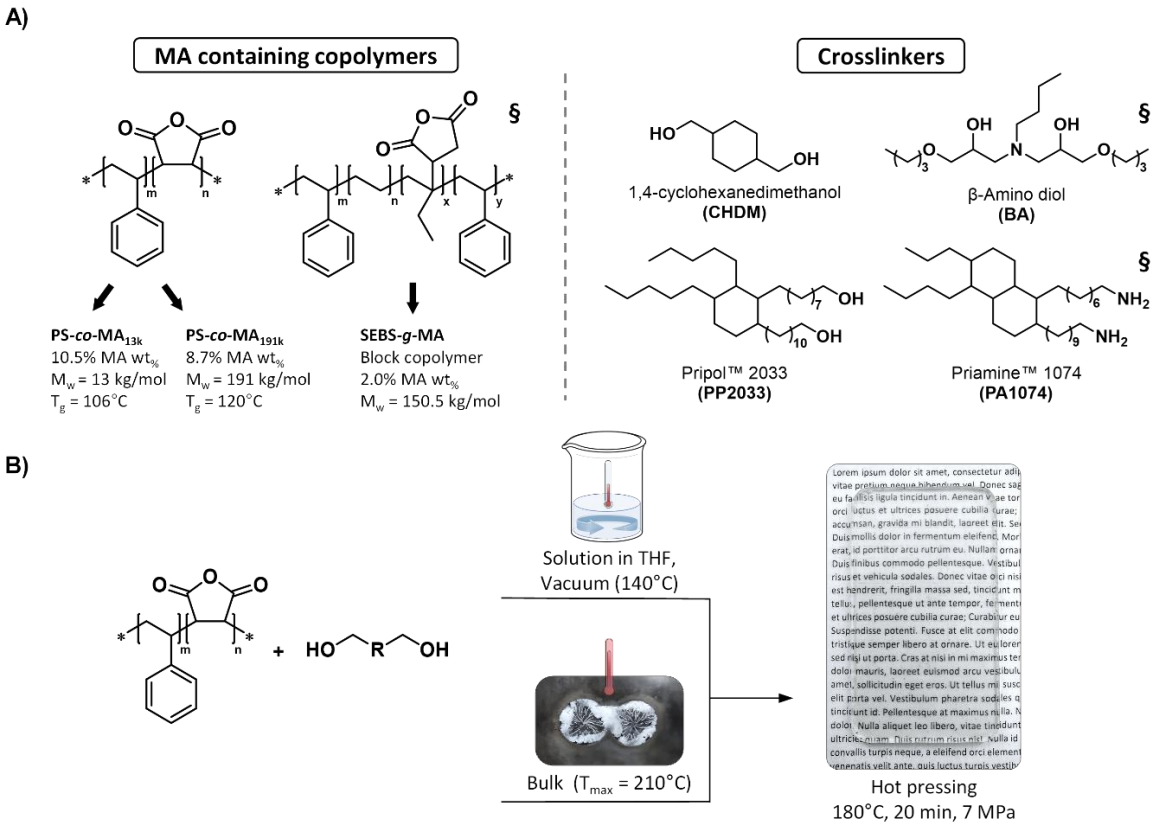

Scheme 2. **A)** (Left) details of the used MA-containing copolymers (**Figure S2**) and (right) crosslinkers used for the synthesis of the studied PS-MMEs. **B)** Scheme of the PS-MME synthesis methods with a picture of PS-MME sample. §Note that these compounds were used to synthesize model networks $\mathbf{G_SPP_{100}}$, $\mathbf{L_SBA_{100}}$ and $\mathbf{H_SPA_{100}}$ (**Table 1**), only to be compared with the PS-MMEs synthesized from the PS-*co*-MAs and aliphatic diols included in this scheme.

Network structural analysis: investigation of the origin of unreacted anhydrides

A deeper understanding of the kinetic and thermodynamic parameters that govern the reversible formation of the MME crosslinks, involving the diols and the MA units embedded into

the PS backbone as 2,3-substituted succinic anhydride moieties, was acquired by FTIR experiments performed on a series of networks with different compositions (**Table 1**).

Table 1. Overview of network formulations, thermal and physical properties of synthesized polymer networks (see Schemes S1-S3).

Network[a]	Precursor polymer	Method	Crosslinker	[OH]/[MA] or [NH_2]/[MA]	T_g[b] (°C)	$T_{d2\%}$[c] (°C)	Swelling ratio (wt%)	Soluble fraction (wt%)
$\mathbf{L_SPP_{100}}$	PS-*co*-MA_{13k}	Solution	PP2033	1.00	80	305	79 ± 3	4.2 ± 0.3
$\mathbf{L_BPP_{100}}$	PS-*co*-MA_{13k}	Bulk	PP2033	1.00	82	310	87 ± 2	5.7 ± 0.5
$\mathbf{L_SCH_{100}}$	PS-*co*-MA_{13k}	Solution	CHDM	1.00	120	270	92 ± 4	4.6 ± 1.3
$\mathbf{H_SPP_{100}}$	PS-*co*-MA_{191k}	Solution	PP2033	1.00	92	330	70 ± 2	1.2 ± 0.5
$\mathbf{H_BPP_{100}}$	PS-*co*-MA_{191k}	Bulk	PP2033	1.00	90	330	74 ± 1	3.2 ± 0.4
$\mathbf{H_SPP_{50}}$	PS-*co*-MA_{191k}	Solution	PP2033	0.50	106	325	90 ± 1	1.6 ± 0.2
$\mathbf{H_SPP_{25}}$	PS-*co*-MA_{191k}	Solution	PP2033	0.25	110	330	130 ± 1	2.2 ± 0.2
$\mathbf{H_SPP_{10}}$	PS-*co*-MA_{191k}	Solution	PP2033	0.10	116	355	170 ± 3	4.8 ± 0.3
$\mathbf{H_BPP_{10}}$	PS-*co*-MA_{191k}	Bulk	PP2033	0.10	117	365	180 ± 7	4.9 ± 1.4
$\mathbf{H_SPA_{100}}$[d]	PS-*co*-MA_{191k}	Solution	PA1074	1.00	118	390	42 ± 1	1.5 ± 0.4
$\mathbf{L_SBA_{100}}$[d]	PS-*co*-MA_{13k}	Solution	PP2033/$BA_{(7/3\ eq.)}$	1.00	91	285	89 ± 3	4.3 ± 0.3
$\mathbf{G_SPP_{100}}$[d]	SEBS-*g*-MA	Solution	PP2033	1.00	-54[e]/ 83[e]	390	210 ± 5	10 ± 1

[a]Systematic $\boldsymbol{A_BC_D}$ labeling codes is explained at the beginning of the present section. [b]Glass transition temperature (T_g) obtained from the second heating run measured by DSC (**Figure S3**). [c]Onset temperature after 2% mass loss measured by TGA (**Figures S6-S7**). [d]These networks were conceived to be compared with the PS-MME networks later in the study. [e]The coexistence of soft polyethylene-*co*-butylene graft maleic anhydride and rigid polystyrene blocks yielded two different glass transition temperatures see **Figure S4**.

Based on the reactivity previously observed for molecular anhydrides and alcohols, the applied curing conditions (140 °C) should give a full conversion of the anhydride moieties into monoesters. Thus, the expectation was that for the stoichiometric networks ([OH]/[MA] = 1.00, see **Table 1**) the characteristic $\nu_{CO,a}$ absorption band of cyclic anhydrides at 1780 cm^{-1} should fully disappear in favor of the formation of two new signals that are corresponding to an intense

$\nu_{CO\ ester}$ band at 1740 cm^{-1} and a weaker intensity ν_{COOH} band at 1710 cm^{-1}. To our surprise, the IR spectra of all stoichiometric PS-MME CANs (**Table 1**) still displayed a remaining and persistent anhydride peak, independently of the molar mass of the PS-*co*-MA precursor or diol used (see **Figures S10-S11**). The correct stoichiometry and reactivity of anhydrides in such conditions were indeed verified by preparing a permanent network with stoichiometric amounts of bisamine crosslinkers (**$H_S PA_{100}$**, see **Table S4** and **Scheme S3.B** for details). In such a case, complete consumption of anhydrides was observed by FTIR (see **Figure S11**).

Hence, unreacted anhydrides in PS-MMEs appear due to the reversible ring opening of the anhydride into monoester, which is key to the dynamic properties of these materials (**Scheme 1.C**). A low equilibrium constant could favor the presence of unreacted anhydrides due to the limited thermodynamic driving force for the ester formation that is unable to overcome the molecular statistical effects hindering full conversion. Such equilibria, involving ring opening, feature significant entropy changes and are thus likely to show a strong temperature dependence. An important aspect to consider is also the high T_g of the styrenic phases (≥ 80°C, see **Table 1**), since their vitrification will 'kinetically arrest'[52] the anhydrides and prevent the re-equilibration of the networks towards the monoester formation upon cooling, maintaining a considerable fraction of dissociated anhydrides preset on any FTIR measured at room temperature. As illustrated in (**Scheme 3.A**), the dissociation of PS-MME crosslinks involves main-chain bond rotations, which are expected to be rapidly hampered as the temperature decreases to values close to the T_g.

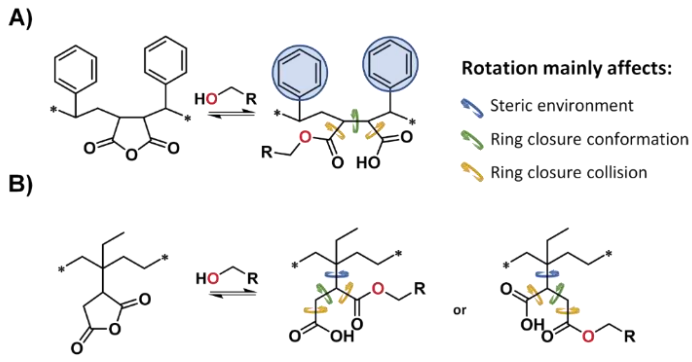

Scheme 3. A) Schematic representation of a MME unit formation from copolymerized MAs in PS-MME networks. B) Schematic representation of a MME unit formation from grafted MAs within GSPP100.

To evaluate whether a kinetically arrested equilibrium could explain the presence of anhydrides at low temperatures, identical samples of $\mathbf{H_SPP_{100}}$ were brought from 200°C to room temperature *via* a fast quenching and a slow cooling rate (below 1 K/min) respectively to have their IR spectra compared. As observed in (**Figure 1**), the quenched material indeed showed a more intense anhydride peak in comparison to the sample that took several hours to be brought to room temperature, similarly to what has been observed by XPS on PS-based dissociative CANs involving 1,2,3 triazolium crosslinks.[14]

With the aim to assess the extent of kinetic inhibition of monoester formation, network $\mathbf{L_SBA_{100}}$ (**Table 1**) was also studied in which a much more reactive diol crosslinker, *i.e.,* a β-amino assisted one, was used (**Scheme S3.C**). There, the tertiary amine functionality within such diol crosslinkers typically results in much faster bond forming and bond exchange reactions with cyclic anhydrides as a result of a double neighboring group participation effect.[34,53] However, although the concentration of unreacted anhydrides got indeed reduced, the curing of $\mathbf{L_SBA_{100}}$ could also not be driven to full completion (**Figure 1**).

While the vitrification effect in PS-*co*-MA chains could effectively hinder the kinetics of crosslink reformation, thermodynamic factors could also contribute as mentioned before (**Scheme 2.A**). To investigate this further, **G_SPP_{100}** was synthesized using the available terpolymer **SEBS-*g*-MA** containing 2 wt% MA (**Scheme S3.A**). This copolymer displays phase separation between glassy PS domains and rubbery ethylene-butene domains (T_g = 83 and -54 °C, respectively) that contain the grafted anhydrides. In such material, grafted MA groups are expected to have milder kinetic restrictions for the anhydrides to reform and for the diols to diffuse and find reaction partners. In line with this reasoning, an almost full conversion could indeed be achieved as shown in **Figure 1**.

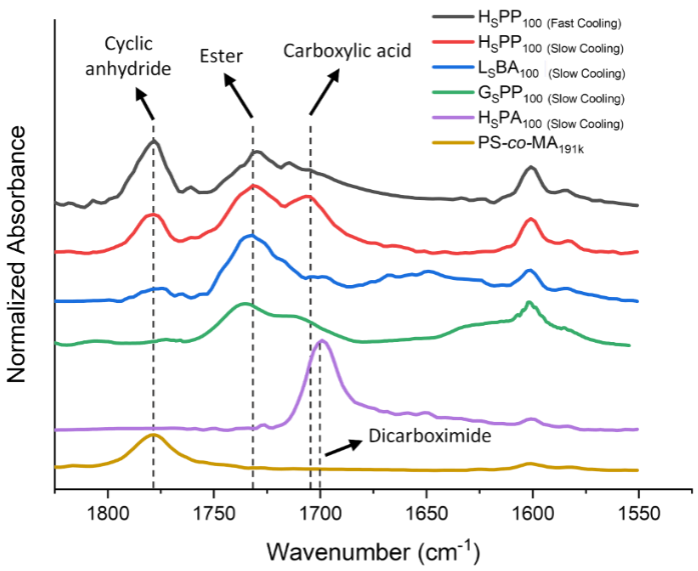

Figure 1. ATR-FTIR spectra of species with individually altered parameters to allow for a comparative study of the final conversion of PS-MME networks (**Table 1**). Reference network **H_SPP_{100}** slowly cooled from 200°C (red), reference **H_SPP_{100}** rapidly cooled from 200°C (black), **L_SBA_{100}** containing beta tertiary amino groups (blue, see **Scheme S3.C**), **G_SPP_{100}** synthesized from a PS and PE copolymer grafted with maleic anhydride (green, see **Scheme S3.A**), permanent **H_SPA_{100}** network crosslinked with dicarboximide bonds synthesized using a bisamine crosslinker (lavender, see **Scheme S3.B**), and dry **PS-*co*-MA_{191k}** used as a network precursor (ochre).

It should be noted that different degrees of remaining unreacted or 'trapped' maleic anhydrides, induced by different cooling rates, also proved to influence thermal properties such as the T_g in networks like **H_SPP_{100}**, observable in DSC experiments (**Figure S5**). Consequently, in order to reduce concentration of unreacted species within the materials and to ensure optimal reproducibility and comparability of the obtained data for different networks, all PS-MME samples were subjected to an hour-long annealing process at 140°C and posterior gradual overnight cooling process at rates below 1 K/min prior to any analysis performed below their T_g. Additionally, since the presence of free alcohols could not be avoided, networks with 50%, 25% and 10% mol content of PP2033 were synthesized using PS-*co*-MA_{191k} as polymer precursor (**Table 1**). In these materials, a large amount of unreacted MA is present at any temperature, regardless of the cooling efficiency or kinetic effects. These less densely crosslinked networks showed comparatively higher T_g values (**Table 1**), as a result of the stiffening caused by the lower amounts of the long aliphatic PP2033 diol (acting as an embedded plasticizer) as can be observed in **Figure S3**.

High temperature FTIR analysis – Assessing the thermal stability of PS-MME CANs

In order to achieve a more comprehensive understanding of the influence of grafted versus copolymerized MA, we studied their dissociation equilibria at elevated temperatures between 80°C and 250°C using high temperature transmission FTIR spectroscopy. Previous investigations pointed towards a dehydrative coupling between free carboxyl functions, resulting in anhydride linkages at elevated temperatures.[47] Therefore, a direct chemical comparison of networks **H_SPP_{100}** and **G_SPP_{100}** was performed to follow significant changes in the molecular structure as well as intermediate or transient species that might emerge with increasing temperature.

In the IR spectra of $\mathbf{H_SPP_{100}}$, the carboxylic acid and ester absorption bands, which are decreasing with temperature, and the simultaneous increasing cyclic anhydride signals can be clearly observed (shown between 100°C and 220°C in **Figure 2.A)**. As the temperature surpassed 140°C, a gradually increasing shoulder at 1755 cm^{-1} was found alongside the MME-related ester signal that decreased in intensity. This carbonyl stretch was never observed during room temperature FTIR analysis despite the elevated temperature treatments performed on every analyzed sample. This observation pointed to an initially overlooked thermally reversible signal that was always necessary to be included for optimal fittings on the performed FTIR deconvolutions, especially at temperatures above 140°C.

This additional band could be attributed to the asymmetric carbonyl stretch of linear (non-cyclic) anhydrides bridging two different chains.[54] Within the given network architecture, a linear anhydride can be achieved by a ring opening reaction between cyclic anhydrides and pendant carboxylic acids, yielding an anhydride bridging across the PS-*co*-MA precursor chains, and making up highly reactive and reversible additional crosslinks (**Figure 2.C**). Once adequate deconvolution parameters were set, high-quality deconvolutions could be obtained (**Figure S15**). Then, the integrated areas of the carbonyl signals were normalized, using the area of the aromatic ring stretch present in every spectrum at 1600 cm^{-1} as a shared internal standard. This allowed for the creation of **Figure S14** as a quantitative measure for the evolution of all described species at specific temperatures. This analysis showed that the formation of such linear anhydride was negligible until 120°C and that their concentration stabilized around 160°C.

As the same analysis was performed on the grafted MA-derived $\mathbf{G_SPP_{100}}$, the lower MA content (2 wt%) resulted in noisier spectra (**Figure S12**), unsuitable to obtain accurate deconvolutions. Nevertheless, a qualitative comparison with its denoised spectra (**Figure 2.B**)

still provides sufficient information to support a qualitative analysis of the thermal differences between **G_SPP_{100}** and **PS-MMEs**. In the spectra of **G_SPP_{100}**, the cyclic anhydride signals increased significantly, even though the carboxylic acid carbonyl signals did not significantly decrease at higher temperatures. Likewise, the ester peak did not decrease significantly upon heating, but rather retained its intensity and broadened, especially above 160°C. Again, a significant shoulder formation could be observed as the temperature surpassed 120°C. This qualitative analysis of **G_SPP_{100}** suggests that linear anhydrides are again being formed like for **H_SPP_{100}** (**Figure 2.A**). However, in contrast to the PS-MME, **G_SPP_{100}** displayed a milder disappearance of carboxylic acids and showed that somehow ester bonds being formed as temperature further increases beyond 160°C.

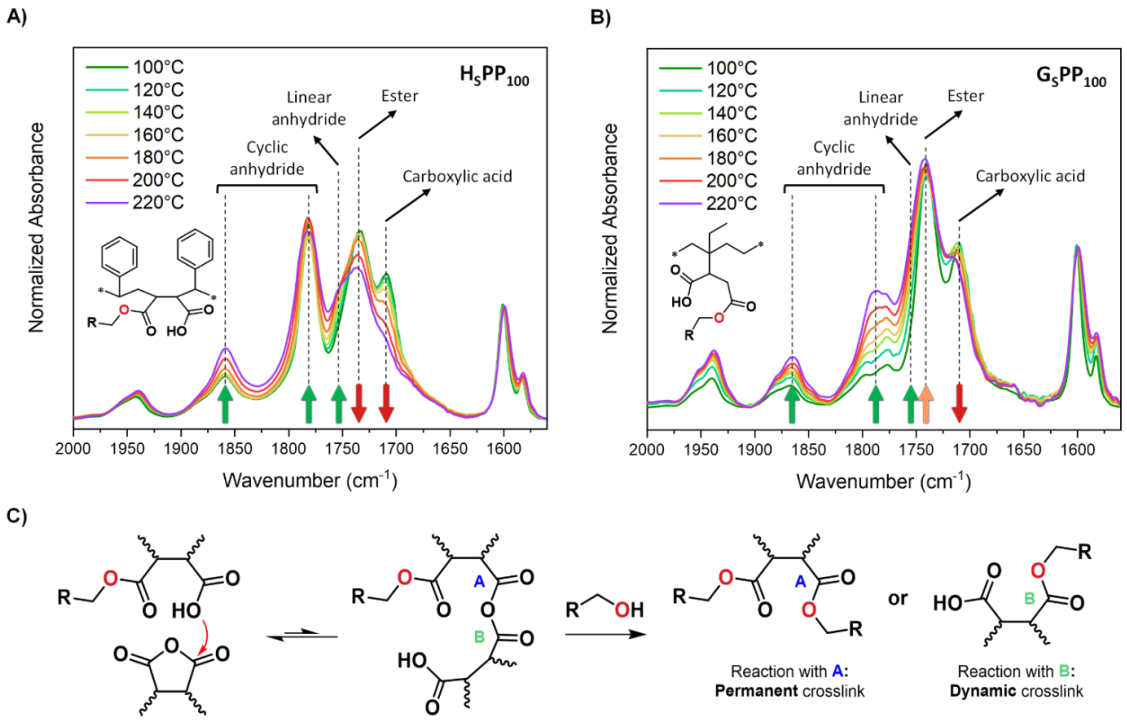

Figure 2. **A)** High temperature spectra of **H_SPP_{100}** with the indicated evolution of its carbonyl stretch peaks with increasing temperature. **B)** Denoised elevated temperature spectra of **G_SPP_{100}** with the indicated evolution of its carbonyl stretch peaks. **C)** Permanent double ester bond formation pathway *via* anhydride bridge intermediates originated in reversible ring openings between carboxylic acids and cyclic anhydrides.

In previous literature on networks containing a high content of cyclic anhydride derived monoesters, a limited thermal stability has been attributed to the formation of head-to-head dehydrative formation of linear anhydrides,[47] resulting in permanent crosslinks. However, exothermic reactions with free hydroxyls would result in an alkyd resin type diester linkage that generally requires temperatures above 200°C (or close to 250°C if no vacuum is applied).[55,56] Thus, as prior studies on phthalate monoester systems[19] and grafted MA-derived MMEs[44–46] employed strict upper temperature thresholds (far below 200°C) in their experiments to avoid permanent crosslinks.[35,57] The neighboring carboxylic acid seems to be the key to this phenomenon, as Heuts and coworkers reported that substitution for a sulfonic acid group seemed to prevent the formation of permanent crosslinks.[35] Based on this high temperature IR study and the observed rheological behavior of PS-MMEs (*vide infra*), we propose an alternative pathway for the formation of permanent diester crosslinks in cyclic anhydride/monoester networks that does not require a condensation of carboxylic acids, but rather a reversible and non-dehydrative ring-opening reaction, initiated by a free carboxylic acid and resulting in asymmetric linear anhydride intermediates bridging across polymer chains. As detailed in **Figure 2.C**, a hydroxyl function could then either react with the formation of a permanent diester crosslink (pathway A) or with the restoration of the MME moiety (pathway B).

It can be expected that the conformationally and sterically more restricted structure of polymerized MAs, present as styrene-maleic anhydride-styrene monomer triads[50,51] within PS-*co*-MAs (**Scheme 3.A**), will less readily undergo these alcoholysis reactions (pathway A and B), thus minimizing the impact of these mechanisms in PS-MMEs. Furthermore, a dehydrative pathway did not seem likely to be operating in PS-MMEs as no significant mass losses below

270°C (**Figure S7**) nor flow property losses were observed (see rheological analysis, *vide infra*), even after long exposures at elevated temperatures (see **Table 1** and **Figure S24**).

Mechanical property analysis of PS-MME CANs

Despite the difficulties in achieving 'full curing' in most networks, the tensile properties PS-*co*-MA_{191k} derived networks (annealed at 140°C *vide supra*) were measured to study the effects of material synthesis conditions and network recycling of computer numerical control machine-cut dog-bones. As observed in the tensile test results (**Figure 3**), all samples with varying amounts of crosslinker (see **Table 1** and **Figure S17**) exhibited stress at break values that were considerably higher than those of the PS-*co*-MA_{191k} or a commercial PS-sample with a M_w of 192 kg/mol (PS_{192k}).

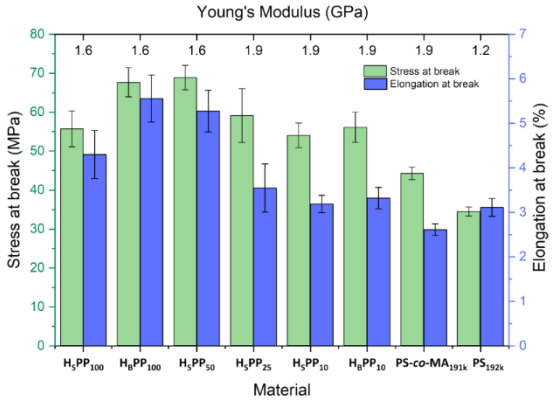

Figure 3. Obtained stress at break (green), elongation at break (blue) and Young's moduli (top) results from uniaxial tensile tests of PS-*co*-MA_{191k} derived PS-MME networks, with PS-*co*-MA_{191k} and a commercial polystyrene of a molecular weight of 192 kg/mol as references (right).

A comparison between $\mathbf{H_BPP_{100}}$ and $\mathbf{H_SPP_{100}}$ CANs synthesized in bulk and in solution respectively, revealed that the former displayed slightly improved mechanical properties. On the other hand, no major differences are observed between $\mathbf{H_BPP_{10}}$ and $\mathbf{H_SPP_{10}}$, suggesting the

absence of a method dependence for networks of lower crosslink densities. In addition, this last result indicates that processing those materials at elevated temperatures in the internal mixer (*i.e.,* 180 to 210°C for at least 5 min, see **Figure S1**) did not induce any loss in mechanical strength. This was a first indication for the excellent thermo-mechanical recyclability of PS-MME CANs. Likewise, it is noteworthy how the low diol loads on $\mathbf{H_SPP_{25}}$ and $\mathbf{H_SPP_{10}}$ were already enough to increment their stresses at break to values 20% and 40% higher than those obtained for un-crosslinked **PS-*co*-MA$_{191k}$** while still yielding soluble fractions below 5% (**Table 2**). Lastly, as expected, the networks' Young's moduli (E) had a proportionally inverse effect on the measured elongations at break of the networks.

Network rheological assessment

The extent of crosslinking at different temperatures, as well as the dynamic behavior of these dissociative networks were further studied by rheological analyses. Small amplitude oscillatory shear (SAOS) experiments of PS-MMEs, conducted between 200°C and 140°C, show three main regimes for all samples (see **Figure 4.A-D** and **Figures S19-S21**)*, i.e.,* ***I***) for low temperatures, an increase of shear storage (*G'(ω,T))* and loss *(G"(ω,T)*) moduli is present at high frequencies, typical for the proximity of the glassy regime; **II**) an apparent plateau in *G'* at intermediate frequencies characteristic for efficiently crosslinked networks (**Figure 4.E**) and ***III***) a relaxation at low frequencies and high temperatures typical of CANs with relatively fast relaxation (*i.e.*, lower than 100 s). In the vast majority of networks, time-temperature superposition does not apply over the complete frequency range, which effectively indicates that the network relaxation obeys distinct temperature dependencies, similar to what has been observed in dissociative PS-based 1,2,3-triazolium dissociative CANs.[14]

First, the *G'* plateau values of all dissociative CANs demonstrate a continuous decrease upon increasing temperature, which is indicative for thermally induced net crosslink dissociation (**Figures S19-S22.B-C**).[36,58] On the other hand, the irreversibly crosslinked network $\mathbf{H_SPA_{100}}$, shows a constant crosslink density and an absence of any relaxation at low frequencies (**Figure S22.A**). Also, only marginal differences can be seen between bulk and solvent-synthesized networks (**B** and **S** series, respectively), which nicely confirms the effectiveness of the aforementioned upscalable preparation using a single batch internal mixer.

At lower temperatures, both networks derived from $\mathbf{PS\text{-}\textit{co}\text{-}MA_{191k}}$ (**H**-series, well above the M_c)[48,49] (**Figure 4.B-C**) and those synthesized from the unentangled $\mathbf{PS\text{-}\textit{co}\text{-}MA_{13k}}$ (**L**-series, below the M_c) (**Figure 4.A**) demonstrate *G'* plateau values that surpass the entanglement moduli of the parent polymer (G_N ~ 200 kPa, see **Figure 4.D-E**), indicating that the network moduli are essentially driven by the formation of MME crosslinks. At 200°C, networks derived from both entangled and non-entangled parent polymers demonstrate a decrease of *G*'. However, this decrease is limited to the entanglement modulus G_N, indicating that the extent of dissociation is not sufficient to result in effective decrosslinking. Only lowly crosslinked samples (*e.g.*, $\mathbf{H_SPP_{10}}$) demonstrate significant thermally induced decrosslinking, as shown by a decrease of their apparent G' plateau significantly below that of G_N (**Figure 4.E**).

In light of these rheological results, it became clear that reaching sufficiently low viscosities for continuous melt (re)processing would require temperatures well above 200°C. The thermal stability and resilience of the sample $\mathbf{PS\text{-}\textit{co}\text{-}MA_{191k}}$ based materials (*e.g.*, $\mathbf{H_SPP_{10}}$) was thus assessed by isothermal TGA-analysis (2 h at 250°C under N_2 flow (**Figure S8**), and successive frequency sweep experiments on the same sample with an atypical duration of *ca.* 105 min run alternatively at 140°C and 250°C (**Figure 4.F**).

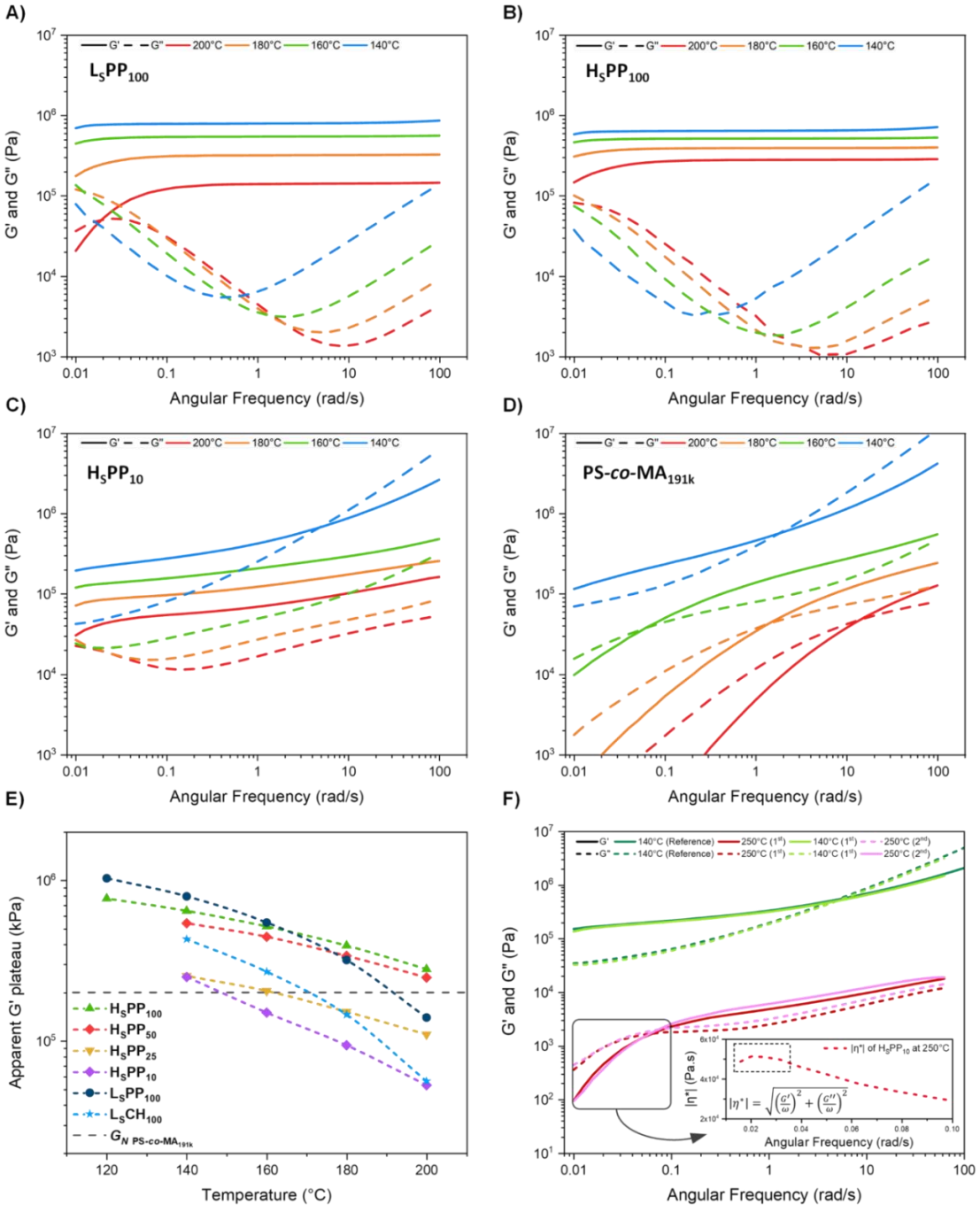

Figure 4. Frequency sweep measurements from 200°C to 140°C showing a decrease in elastic modulus with increasing temperature of: **A) L_SPP_{100} B) H_SPP_{100} C) H_SPP_{10} D) PS-*co*-MA_{191k}. E)** Apparent *G'* plateau values as a function of temperature of all in-solution synthesized networks with the G_N of **PS-*co*-MA191k** as reference. **F)** Frequency sweep measurements of **H_SPP_{10}** measured on the same sample on alternating runs at 140°C and 250°C, including a close-up of the complex viscosity ($|\eta^*|$) plateau reached on the terminal zone at low frequencies.

In contrast to other PME[19] or MME-based[44–46] systems, the recorded small mass loss (< 1 wt%), together with an absence of any significant *G'* and *G"* deviations observed after being exposed at such elevated temperatures, demonstrate that PS-MME CANs hold a remarkable thermal stability and resilience that does not compromise their integrity nor rheological properties.

As the analysis of dynamic network relaxations at low frequencies using SAOS is rather complex, temperature dependent stress relaxations were performed between 160 and 210°C. The relaxation moduli *G(t)* were monitored for at least one complete decade of relaxation, over durations ranging from 1000 to 10,000 s (**Figures S35-S36**). When possible, representative relaxation times (τ) were extracted by fitting the relaxation moduli for each temperature with a Kohlrausch−Williams−Watts (KWW) stretched exponential decay[8,14,62,63] (see equation *(S1)* on SI file for detailed information). The values of network moduli $\boldsymbol{G_0}$ were taken at the plateau, typically designated as $\boldsymbol{G_0} = \boldsymbol{G}$(1 s). However, as it will be further discussed below, we also determined the continuous relaxation spectra from the stress relaxation curves and proposed a more detailed analysis of the distribution of relaxation times, extracted from their Continuous Relaxation Spectrum (CRS)[64–66] rather than from a single averaged value (**Table 2**).

The thermal stability of the samples during the measurements and the reversibility due to temperature variations were confirmed using $\mathbf{L_SCH_{100}}$ (with the lowest $\boldsymbol{T_{d2\%}}$) by repeating up to four different cycles of temperature steps between 150°C and 200°C, showing only minimal changes (**Figure S24**). PS-*co*-MA networks incorporating β-amino alcohol crosslinkers ($\mathbf{L_SBA_{100}}$) and SEBS-*g*-MA networks incorporating Pripol crosslinkers ($\mathbf{G_SPP_{100}}$) were examined in similar conditions (**Figure S25**). In both cases, irreversible side reactions lead to an

increase of the moduli and of relaxation times, demonstrating significantly impaired flow properties.

A strategy to complement the measurements of relaxation times of these CANs is the assessment of creep viscosities, which are not solely dependent on relaxation time but also on the effective variation of their moduli with temperature. Such analysis provides critical insight on the effective network connectivity.[14,59–61] Thus, creep tests at different temperatures were performed in the linear regime, under constant shear stresses (σ) of 1 or 2 kPa. From them, creep compliances ($J(T,t) = \gamma(T,t) / \sigma$) were analyzed in the apparent steady viscous flow regime to estimate the zero shear viscosities (η_0) (see details in Supporting Information and **Figure S34**).[14,67]

When the unentangled **PS-*co*-MA$_{13k}$** was used as network precursor (with a molar mass below M_c), the resulting CANs (**L**-series, see **Figure 5.A** and **Figure S26**) showcased fast relaxation ($\tau_{200°C}$ < 30 s, **Table 2**) as extracted from KWW exponential decay fittings ($G(t,T) = G_0.e^{-\left(\frac{t}{\tau^*}\right)^{\beta}}$). This resulted in nearly monomodal relaxations in the full temperature range (160 to 200°C), characterized by β parameters close to 1 (from 0.7 to 0.8 **Table S6**), as well as a significant decrease of modulus between 160 and 200°C, down to 30 kPa (**Figure 5.A** and **Table 2**). The corresponding temperature-dependency of relaxation times conform closely to a single Arrhenius model ($\tau(T) = A_\tau.e^{\frac{E_{a,k}}{RT}}$) with $E_{a,k}$ being the kinetic activation energy. Pripol 2033- and CHDM-based networks exhibit similar $E_{a,k}$ values (*ca.*, 125 kJ mol^{-1}), indicating that all relaxations are driven by the same chemical events, *i.e.*, dissociation and re-formation of MMEs occurring on crosslinked networks.

Table 2. Rheological properties of PS-MME networks obtained *via* stress relaxation and creep measurements.

Material	$G_{0(200°C)}$ [a] (kPa)	$G_{0(160°C)}$ [b] (kPa)	$\tau_{200°C}$ [c] (s)		$T_{160°C}$ [c] (s)		$E_{a,k}$ [d] (kJ mol^{-1})		$E^{I}_{a,v}$ [e] (kJ mol^{-1})	$E^{II}_{a,v}$ [f] (kJ mol^{-1})
			KWW	CRS	KWW	CRS	KWW	CRS		
L_SPP_{100}	29	325	16	17	288	290	124 ± 2.4	119 ± 2.4	-	136 ± 1.7
L_BPP_{100}	30	390	15	15	248	250	119 ± 5.3	122 ± 9.5	-	124 ± 1.9
L_SCH_{100}	98	500	34	38	750	893	129 ± 1.0	131 ± 2.9	-	174 ± 3.5
H_SPP_{100}	190	390	123	91	1454	785	105 ± 5.2*	92 ± 1.9	47 ± 0.7	93 ± 2.5
H_BPP_{100}	130	280	117	91	1141	679	96 ± 2.2*	84 ± 2.4	66 ± 2.2	101 ± 2.8
H_SPP_{50}	230	390	173	96	2012	1069	98 ± 4.6*	83 ± 5.7	57 ± 1.1	137 ± 2.5
H_SPP_{25}	100	230	104	118	1350	1255	104 ± 3.8	95 ± 4.3	118 ± 4.5	211 ± 7.4
H_SPP_{10}	80	240	89	124	905	1401	102 ± 2.9	102 ± 1.9	128 ± 1.8	299 ± 2.2
H_BPP_{10}	80	300	51	96	513	1177	106 ± 3.4	108 ± 2.3	131 ± 2.2	298 ± 24
PS-*co*-MA_{191k}	-	-	-	-	-	-	-	-	-	300 ± 10*

[a,b]Network $G(t,T)$ values assuming: $G_0 = lim(t\rightarrow 0+)\ G(t,\ T)$; taken at plateau values at 200°C and 160°C, respectively. [c]Relaxation times τ at 200°C obtained from the fitting with KWW model equation *(3)*. [d]Kinetic activation energy ($E_{a,k}$) of the stress relaxation of the network calculated from the KWW fittings and CRS $H(\lambda)$ maxima *(3)*. [e]Viscous flow activation energies ($E_{a,v}$) of networks on the flow *regime I* calculated by fitting their zero shear viscosities ($\eta_0(T)$) to equation *(S4)*. [f]Viscous flow activation energies ($E_{a,v}$) of networks on the flow *Regime II* calculated by fitting their zero shear viscosities ($\eta_0(T)$) to equation *(S4)*. *Note that the lower quality of the KWW fittings used to calculate these $E_{a,k}$ render these values less accurate to any value obtained from the τ distribution analysis.

In contrast to the unentangled samples, the longer PS-*co*-MA chains (above the M_c) bearing more MA units per chain, are expected to result not only in chain entanglements,[68] but also in more efficiently crosslinked chains,[8] hampering the stress relaxation phenomena at lower temperatures. Thus, CANs obtained from entangled **PS-*co*-MA_{191k}** (**H**-series, see **Figure 5B** and **Figure S27**) displayed relaxations with significantly broader distributions that could not always be effectively captured with stretched KWW exponential decays across all temperatures (**Figure S27.A-C**). The presence of slow relaxation modes becomes particularly obvious at temperatures

lower than 180°C in highly crosslinked networks incorporating over 50 mol% crosslinkers (e.g., $\mathbf{H_BPP_{100}}$ to $\mathbf{H_SPP_{50}}$). Such materials denote a temperature dependent relaxation regime that renders conventional rheological tools such as time-temperature superposition (TTS) ineffective.[22,63] At 200°C, a reasonably well fitting with stretched exponentials can be achieved. The corresponding relaxation times ($\tau_{200°C}$ =120 s for $\mathbf{H_SPP_{100}}$) increase up to eightfold in comparison to that of the unentangled PS-MME analogues. Notably, a significant decrease of relaxation times is also seen when the extent of crosslinking is decreased from $\mathbf{H_SPP_{50}}$ to $\mathbf{H_SPP_{10}}$ as expected.

However, it should be noted that at lower temperatures, slow relaxation modes alter the relaxation profiles and are rather captured by a power law than by exponential decays. For this, we refer to **Figure 5B** where sample $\mathbf{H_BPP_{100}}$ at 160°C and 170°C decays in particular as $G(t)\sim t^{-0.46}$ and $G(t)\sim t^{-0.52}$ respectively. In fact, the theoretical description of relaxation phenomena in entangled dynamic polymer networks can be rationalized through the Sticky reptation model by Leibler, Rubinstein, and Colby.[24] This model delineates relaxation events based on critical timescales: the Rouse time of an entanglement strand (τ_e), the lifetime of dynamic bonds (τ_{bond}), and the terminal relaxation time of the network (τ_R). At low crosslink density and slow dynamic exchanges ($\tau_{bond} > \tau_e$), dynamic bonds and entanglements jointly determine the network moduli. This significantly delays relaxation (τ_R), which is governed by the bond lifetime and topological features such as chain size and crosslink density.

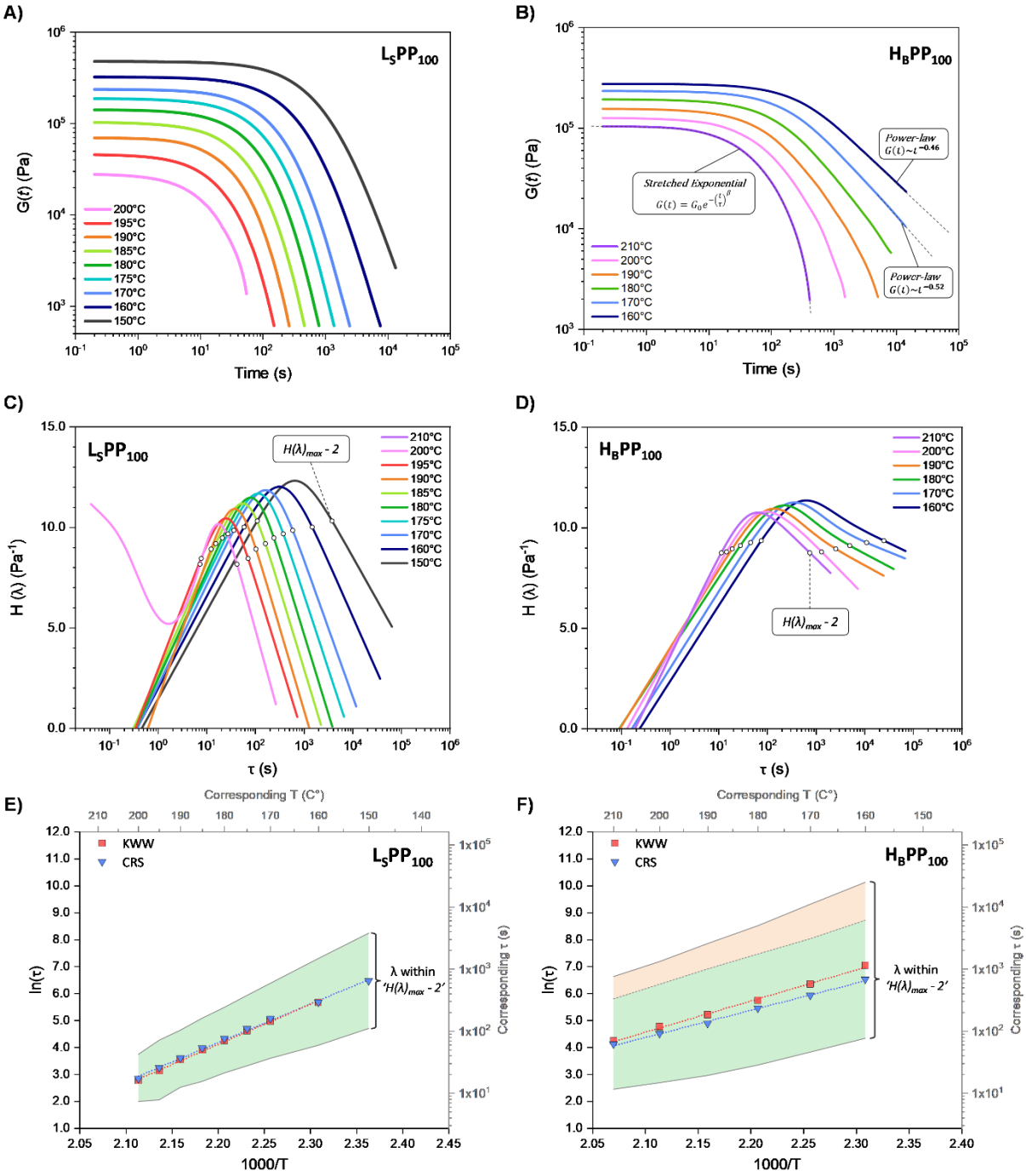

Figure 5. **A)** Stress relaxation results of $\mathbf{L_SPP_{100}}$ synthesized from unentangled PS-*co*-MA precursor. **B)** Stress relaxation results of $\mathbf{H_BPP_{100}}$ synthesized from a PS-*co*-MA precursor of high molar mass. **C)** Relaxation time distributions extracted from the CRS 'PyReSpect' fit of the stress relaxation experiments performed on $\mathbf{L_SPP_{100}}$. **C)** Relaxation time distributions extracted from the CRS fit of the stress relaxation experiments performed on $\mathbf{H_BPP_{100}}$. **E)** Stress relaxation Arrhenius plots of network $\mathbf{L_SPP_{100}}$ extracted from the single Maxwell stretched exponential decay (KWW) model fittings and CRS maxima (**Table 2** and **Figures S26-S29**). **E)** Stress relaxation Arrhenius plots of network $\mathbf{H_BPP_{100}}$ extracted from the single Maxwell stretched exponential decay (KWW) model fittings and CRS maxima (**Table 2** and **Figures S26-S29**).

This model was later extended by Ricarte and Shanbhag to decouple the interactions between modes of relaxation, associated with regular segments and "sticky" segments.[69] Their simulations focused on highly entangled polymers and led to the prediction of distinct regimes in the time evolution of relaxation moduli: *I*) initial Rouse dynamics transitioning from the glassy state to the rubbery state and following a power-law decay with $t^{-1/2}$, *II*) a rubbery plateau modulus depending on the effective formation of dynamic bonds, that extends with the density of crosslinks and the lifetime of dynamic bonds, *III*) then a second power-law decay, also with $t^{-1/2}$ linked to the initial Rouse dynamics through a reptation model and finally *IV*) a terminal relaxation beyond which the modulus decays mono-exponentially.

To the best of our knowledge, experimental evidence has not yet consistently supported the presence of regime *III*, even if some numerical models including reptation phenomena highlighted the presence of a regime *III* with a slope $G(t) \sim t^{-1/2}$ as characteristic of dynamic network relaxation.[70–72] While our data do not exhibit clearly separated relaxation modes *II* and *III*, they rather suggest entangled PS-MMEs transition from a power-law trend towards a nearly monoexponential stretched decay ($\beta \geq 0.7$) upon temperature increase. Then, the presence of nearly monoexponential network relaxations in some cases suggests that the terminal relaxation in PS-MMEs is primarily determined by the lifetime of bonds τ_{bond}, and that no intense reptation mechanism is longer associated to it. This situation corresponds to both unentangled materials (**L**-series) and entangled materials (**H**-series) at high temperatures or of lower crosslink densities (e.g., $\mathbf{H_SPP_{25}}$ and $\mathbf{H_SPP_{10}}$). For entangled systems at lower temperatures, where reptation times are higher, the relaxation moduli rather follow powerlaw decays; thus indicating an effective interplay between Rouse dynamics and covalent bond exchanges.

Consequently, the KWW stretched model (while very useful for fitting relaxation curves featuring a narrow relaxation time distributions) does not accurately capture some of our experimental data due to the presence of Rouse regimes *I* (**Figure S27.E-F**) or *III* (**Figure S27.A-D**). An alternative strategy for analyzing relaxation data based on the complete relaxation spectrum is thus necessary. Different methods have been well established over the years, such as discrete models featuring multiple exponential modes (*e.g.*, the generalized Maxwell model), or continuous models aiming to obtain the complete shape of the relaxation spectrum. Mathematically, determination of the relaxation spectrum is an ill-conditioned problem with strong numerical instability in the presence of low-precision data. This has been conventionally solved using regularization data processing codes that impose a smooth-shaped solution based on the CONTIN algorithm developed by Provencher in the 80s.[73] This seminal code was later ported to different programming languages and operating systems, and the regularization conditions fine-tuned to distinct analytical requirements. The 'PyReSpect' model, for instance, processes rheological stress relaxation data into Continuous Relaxation Spectra (CRS) while ensuring that the minimum amount of distinct relaxation modes are used (**Figures S28-S29**).[64,74]

The resulting CRS, referred to as $H(\lambda)$ (**Figures S30-S31**), represent the distribution of relaxation strengths[75] as a function of the relaxation times λ. This shows how the relaxation is dominated by a single relaxation mechanism[65,66] from which the τ_{CRS} assigned to the $H(\lambda)$ maxima were utilized to construct the CRS Arrhenius plots and to calculate their respective CRS $E_{a,k}$ values as seen in **Table 2** and **Figure S32**. However, in view of how the CRS of entangled materials significantly broaden and skew towards slower relaxation modes (*e.g.*, $\mathbf{H_BPP_{100}}$ and $\mathbf{H_SPP_{50}}$ at low temperatures), a single averaged $\tau_{KWW\ or}\ \tau_{CRS}$ value seemed to be insufficient to properly characterize the relaxation dynamics of entangled materials. Therefore, λ ranges were

constructed, selecting values comprised within '$H(\lambda)_{max}$ - *2*' and were overlayed in the Arrhenius plots (**Figure 5.E-F and Figure S32**) to represent the relaxation time distributions of PS-MMEs. On the one hand, the λ areas resulting from unentangled systems (shown as green areas between the solid gray lines in **Figure 5.E** and **Figure S32.A-C**), revealed symmetric λ distributions centered in CRS Arrhenius plots.

On the other hand, the *H(λ)* positive skewness observed in entangled systems led to λ ranges that are not centered in the CRS but rather in the KWW Arrhenius plots. There, the Rouse dynamics resulted in an additional range of slow relaxation events that broadens as temperature decreases (shown as orange areas in **Figures 5.F** and **Figure S32.D-F**). Additionally, in the case of **L**-series materials (*e.g.*, $\mathbf{L_SPP_{100}}$ or $\mathbf{L_SCH_{100}}$) the τ and $E_{a,k}$ values (**Table 2**) practically overlay, independently of the method used (KWW or CRS). Conversely, in highly entangled systems (*e.g.*, $\mathbf{H_BPP_{100}}$ and $\mathbf{H_SPP_{50}}$), the KWW values deviate towards higher values due to the positive skewness of the relaxation time distributions. Furthermore, as observed in KKW fits performed on materials from the **H**-series with lower crosslinker loads (*i.e.*, $\mathbf{H_SPP_{10}}$ and $\mathbf{H_BPP_{10}}$ in **Figures S29.E-F**), intense initial Rouse decays in regime *I* render the KWW fittings to be less precise and deviate from the CRS results (**Table 2**, **Figure S33**). This evidences how CRS not only serves to extract high quality relaxation data from such non-monoexponential curves, but also allows the calculation of τ and $E_{a,k}$ values that are independent of the skewness induced by Rouse reptation mechanisms in regime III, while also revealing how they broaden the resulting λ distributions.

Given the presence of slow relaxation modes and broad relaxation time distributions, assessing shear viscosities (η_0) close to the terminal regime is best achieved through extended creep

experiments over 5000 s (see **Figure S25**). There, unentangled CANs (**L**-series, **Figures** 6A and **Figure S36**) demonstrated a single Arrhenius dependency of viscosity across the entire temperature range, which is consistent with simultaneous decreases in relaxation times and crosslink density with increasing temperature. The corresponding viscous flow activation energy $\boldsymbol{E_{a,v}}$ could be calculated following: $\eta_0(T) = A_\eta . e^{\frac{E_{a,v}}{RT}}$.

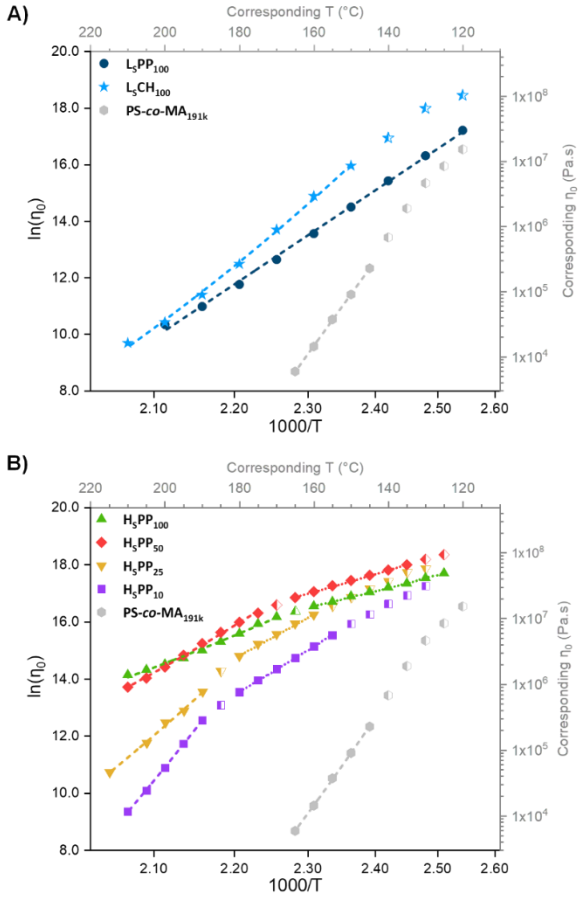

Figure 6. **A)** Arrhenius plot of the zero-shear viscosity evolution calculated from creep experiments of networks synthesized from low molecular weight PS-*co*-MA precursor and **PS-*co*-MA$_{191k}$** as reference. **B)** Arrhenius plot of the zero-shear viscosity evolution calculated from creep experiments of networks synthesized from **PS-*co*-MA$_{191k}$** precursor with **PS-*co*-MA$_{191k}$** as reference where the half full symbols denote non-linear regions transitioning towards a different flow regime.

In contrast, CANs from entangled PS-*co*-MA precursors (**H**-series) displayed tow main regimes, characterized by different slopes when plotting $\ln(\eta_0)$ vs $1/T$ (**Figures 6B**). Dissociative CANs are theoretically capable of transitioning across four different viscoelastic flow regimes upon increase of temperature: *R-I*) dynamic networks with constant crosslink density, *R-II*) dynamic networks with crosslink densities decreasing at high temperatures, *R-III*) dynamic networks undergoing gel-sol transition as the net fraction of crosslinks decays below a critical value, *R-IV*) fully decrosslinked networks behaving as the parent precursors.[14] In the studied temperature range, all dissociative networks typically display a R-II regime, as evidenced by the moderate variation in network moduli by a factor < 5. The evolution of $\boldsymbol{\eta_0}$ with temperature can thus be attributed to the combination of variations in the relaxation times and thermally induced decrosslinking.

While direct comparison of stress relaxations results using a single set of relaxation time values proved to be more complex for entangled systems, the creep viscosities provide a useful comparison of their *near-terminal* flow behaviors, which will admittedly be strongly driven by slow relaxation modes. We reported the discrete $E_{a,v}^{I}$ and $E_{a,v}^{II}$ viscous flow activation energies found at low and high temperatures respectively (**Table 2**). Whereas all systems display expected viscosities converging to very high values close to 10^8 Pa s in proximity to their T_g, entangled crosslinked networks show significantly lower $E_{a,v}^{I}$values at low temperatures, which results in much higher viscosities in the 140-180°C range. The viscosities also increase strongly with the crosslink density of the networks between 170 and 190°C. Entangled networks enter a second regime with much higher $E_{a,v}^{II}$values, ranging from ca. 90 to 140 kJ mol^{-1} for highly crosslinked samples to 200 to 300 kJ mol^{-1} for weakly crosslinked samples. It is interesting to note that the value of 300 kJ mol^{-1} is also found for the precursor **PS-*co*-MA$_{191k}$** and appears to correspond to

a truly terminal regime. By analogy with the discussion above regarding distinct relaxation mechanisms, we attribute the $E_{a,v}^{I}$ and $E_{a,v}^{II}$ values to regimes where interplay between reptation and dynamic crosslink exchanges occurs,[59–61] and where only dynamic crosslink exchanges drive the viscoelastic behavior. In order to coherently present the data of unentangled systems , we attributed their unique $E_{a,v}$ value to the $E_{a,v}^{II}$ that corresponds to the reptation-free regime. Interestingly, while in the former case, variations of $E_{a,v}^{I}$ are only moderate in the 50-90 kJ mol^{-1} range, variations of $E_{a,v}^{II}$ in the latter case can vary dramatically from 90 to 300 kJ mol^{-1} depending on the crosslink density. Such evolutions appear tightly connected to the effective connectivity of the networks. Moreover, this will understandably decrease faster upon increase of temperature for low molar mass precursors that feature weakly crosslinked chains, highlighting their insufficient crosslink densities and lower energies required to facilitate flow.

Single Screw Extrusion and Injection Molding – (Re)processing of PS-MMEs

Given the high thermal resilience and excellent flow properties of PS-MMEs, the next objective was the exploration of continuous (re)processing methods. In this context, despite their faster flowability, materials derived from PS-*co*-MA_{13k} were not further investigated because of their lower degradation temperatures, abrupt viscosity reductions and poor mechanical properties. As the processing of **PS-*co*-MA_{191k}** based PS-MMEs required elevated temperatures, an isothermal thermogravimetric analysis (TGA) was conducted at 250°C for a duration of two hours. There the network exhibited minimal mass loss, retaining more than 99% of its initial mass (**Figure S8**). Since **H_SPP_{10}** proved to be the fastest flowing material and displayed not only a low soluble fraction but also enough solvent resistance at low temperatures (**Figure 7**), **H_SPP_{10}** and **H_BPP_{10}** were selected for the extrusion experiments. Prior to actual single screw extrusion,

their extrusion feasibility was confirmed by analyzing the melt flow index (MFI) of $\mathbf{H_SPP_{10}}$ at 250°C (see section 11 on SI for detailed information).

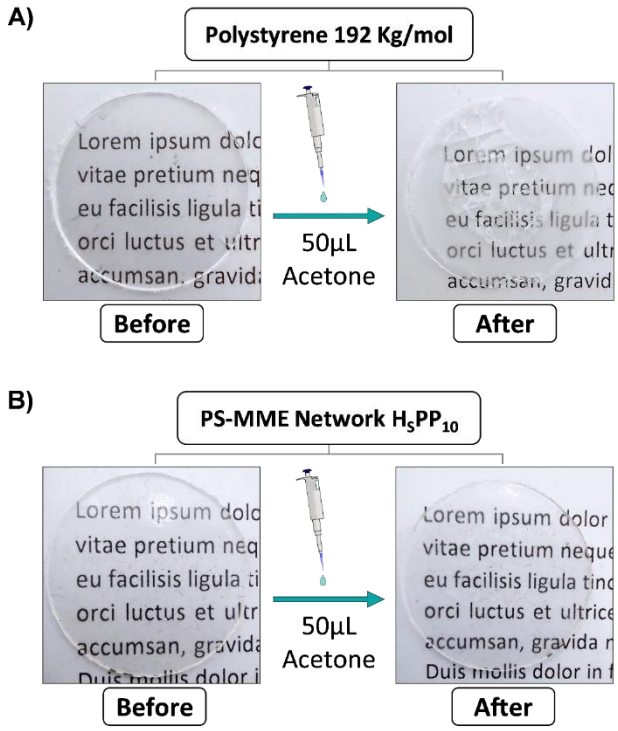

Figure 7. Pictures before (left) and after (right, 24h at 21°C) adding a drop of 50 µL of acetone on the surface of samples 22mm in diameter and 0.1mm thick of **A)** PS (192 kg/mol) and **B)** network $\mathbf{H_SPP_{10}}$. As can be observed, unlike the PS, $\mathbf{H_SPP_{10}}$ showed no surface cloudiness or crack formation defects.

The extrusion of $\mathbf{H_SPP_{10}}$ and $\mathbf{H_BPP_{10}}$, fed as granules with an approximate diameter between 0.5 to 1.0 mm, was performed without thermal stabilizers using a custom-built single screw mini-extruder (**Figure S38.B**). Initial experiments were conducted at 210°C with a 1.0 mm diameter die, protruding the extruder's barrel heating jacket (**Figure 8.A**). As demonstrated in the (see supporting **Video 1**), continuous extrudates with a diameter of 1.85 ± 0.04 mm (**Figure 8.B**) were produced for both $\mathbf{H_SPP_{10}}$ and $\mathbf{H_BPP_{10}}$ with 85% post-extrusion swell and minimal yellowing (**Figure 8.C**). Additionally, while covering the die with the heating jacket, hot drawing experiments were conducted at 250°C using a spinning device (see supporting **Video 2**),

yielding continuous filaments with a minimal diameter of 0.25 mm (**Figure 8.D**). No major superficial defects were observed at extrusion temperatures ranging from 210°C to 250°C for $\mathbf{H_SPP_{10}}$ and $\mathbf{H_BPP_{10}}$ and their thermal properties, swelling degrees and soluble fractions remained comparable to the values obtained for samples obtained *via* hot pressing (for both in solution and in-bulk synthesized PS-MMEs, **Table S9**). Thus, the combination of favorable post-extrusion property retention and efficient drawability (attributable to a low extensional viscosity) demonstrates that such dissociative networks are suitable for advanced thermoplastic processing tools like blow molding or blown film extrusion. In view of these successful results, the suitability of both $\mathbf{H_SPP_{10}}$ and $\mathbf{H_BPP_{10}}$ to be processed through injection molding processes was finally evaluated using a lab-scale injection machine as a proof of concept study (**Figure S39**), operating at an injection pressure of 8 bar. Preheated samples (2 min, 260°C) were effectively injected to the mold (80°C) yielding clear rectangular shapes (63.5 mm x 12.5 mm x 3.15 mm, **Figure 8.E**) within a combined injection and cooling time of 12 s.

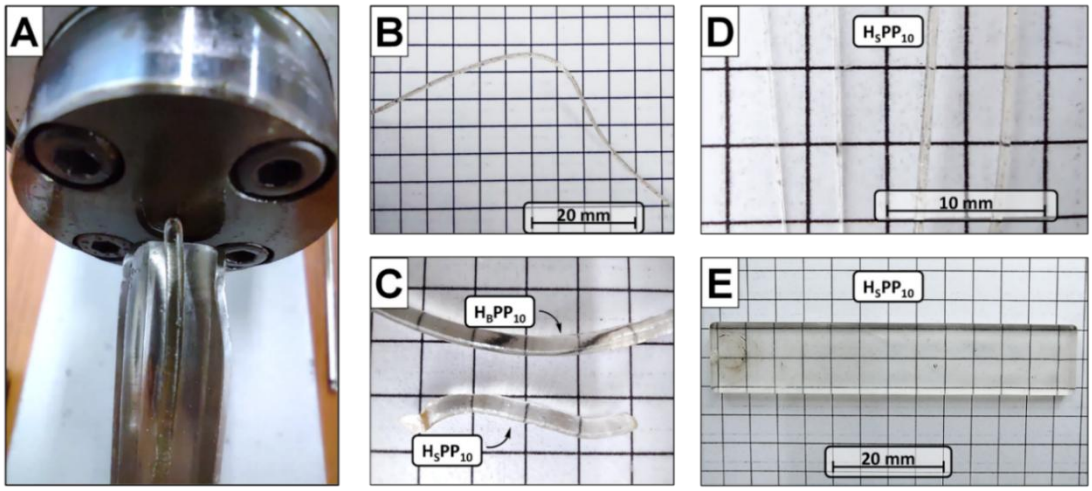

Figure 8. **A)** Picture of the extrusion of $\mathbf{H_SPP_{10}}$ performed at 210°C. **B)** Picture of a $\mathbf{H_SPP_{10}}$ homogeneous extrudate. **C)** Close-up picture of $\mathbf{H_SPP_{10}}$ (bottom) and $\mathbf{H_BPP_{10}}$ (top) extrudates. **D)** Picture of hot-drawn $\mathbf{H_SPP_{10}}$ filaments where different constant diameter sizes are displayed. **E)** Picture of a $\mathbf{H_SPP_{10}}$ homogeneous and clear bar (63.5 mm x 12.5 mm x 3.15 mm) injected at 260°C into the rectangular mold at 80°C.

Chemical Recycling of PS-MMEs

Processes with the aim of recovering and repurposing the starting components have gained considerable attention over the last decade.[76–80] Therefore, in addition to the physical recycling *via* single screw extrusion and injection molding discussed above, we targeted a chemical recycling process with the aim to recover both the diol crosslinker and the PS-*co*-MA precursor or to regenerate the PS-MME network. After isolation and purification, these could be repurposed or used again to resynthesize pristine PS-MMEs. It is notable that all PS-*co*-MA_{191k} derived networks proved to be soluble in hot xylene, indicating extensive decrosslinking (**Figure S40**). For this part of the study, 10 g of $\mathbf{H_SPP_{10}}$ was dissolved in 300 mL of xylene *via* soxhlet extraction (**Scheme 4.A-B,** see SI section for further details). The obtained solution (33.2 mg/mL) was subsequently divided into three aliquots to be used for separate procedures.

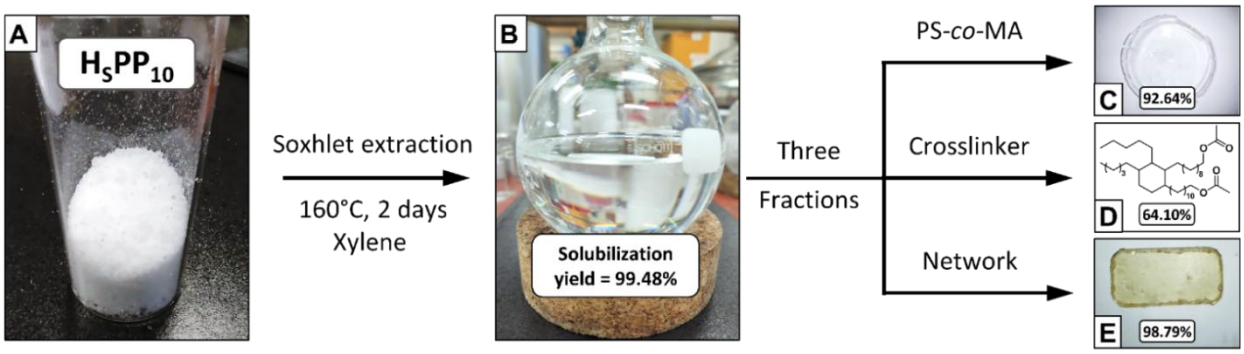

Scheme 4. Schematic representation of the chemical recycling experiments performed on $\mathbf{H_SPP_{10}}$. A) Fine shredded $\mathbf{H_SPP_{10}}$ sample used in the study. **B)** $\mathbf{H_SPP_{10}}$ solubilized in xylene after the Soxhlet extraction. **C)** Retrieved PS-*co*-MA_{191k} sample. **D)** Separated (predominantly) acetylated form of PP2033. **E)** Recycled $\mathbf{H_SPP_{10}}$ from its solution in xylene.

Two 75 mL fractions were treated to isolate the two constituents from the network (**Scheme 4.C-D**), whilst the third demonstrator experiment was aimed at regenerating the network straight from the solution by solvent removal and direct re-curing (full detail of the procedures can be

found in the SI). The retrieved PS-*co*-MA copolymer was then reused in the synthesis of a PS-MME network (**Scheme 4.C**).

After its purification by iterative precipitations in cold diethyl ether, the precursor polymer could be recovered in more than 90% yield. Moreover, no notable variations in FTIR spectra were detected between the original and recycled PS-*co*-MA (**Figure S42**). The sole discernible difference could be detected *via* GPC analysis, indicating a rise in the chromatogram region associated with elevated molecular weight chains (**Figure S2**), an outcome attributed to chain couplings arising from diol traces not observable *via* FTIR. Then, the synthesis of $\mathbf{H_SPP_{10}}$ was repeated by combining the isolated PS-*co*-MA with a diol while the properties of the obtained network were compared with pristine $\mathbf{H_SPP_{10}}$. All FTIR, DSC, TGA frequency sweep and creep experiments (**Figures S42-S46** and **Table S9**) pointed towards a higher crosslink density in the network with recycled **PS-*co*-MA$_{191k}$**, exhibiting properties closer to $\mathbf{H_SPP_{25}}$ than those of $\mathbf{H_SPP_{10}}$. These results indicate the presence of residual crosslinker in the recuperated precursor polymer due to an incomplete (physical or chemical) separation of PP2033 from the polymer chains. In principle, this could be swiftly corrected with the addition of virgin **PS-*co*-MA$_{191k}$**. Likewise, it can be expected that further optimization of the separation procedure could increase the **PS-*co*-MA$_{191k}$** and diol separation efficiency.

From the second $\mathbf{H_SPP_{10}}$ 75mL aliquot, a quantitative retrieval of a partially acetylated form of PP2033 was performed by treating the xylene solution with acetyl chloride and separating the dissolved PS-*co*-MA by precipitation in MeOH (**Scheme 4.D**). The resulting oil was then compared through ^{1}H-NMR with a fresh PP2033 sample subjected to the same acetylation procedure (64.1% yield calculated including the residual monoacetylated and/or non-acetylated

PP2033 observed by ^{1}H-NMR as seen in **Figure S47**). The obtained oil could be repurposed or used to regenerate the original alcohols *via* ester hydrolysis. Lastly, a network re-curing experiment was performed using the remaining 150 mL of $\mathbf{H_SPP_{10}}$ solution by simply concentrating and drying it, following the original solution synthesis procedure described for PS-MMEs (98.8% yield). The resulting materials could be hot-pressed (**Scheme 4.E**), analyzed and have their properties compared with those of the original $\mathbf{H_SPP_{10}}$. In contrast to the network that was resynthesized from the recuperated **PS-*co*-MA$_{191k}$**, the analyses of the re-cured material (**Figures S42-S46**, **Table S9**) pointed towards a network with comparable properties to $\mathbf{H_SPP_{10}}$. The sole difference is a slightly lower crosslink density, as can be deduced from the lower η_0 and apparent *G'* plateaus, ascribed to diol loss during the recycling process that could be compensated by adding extra PP2033 during the synthesis step.

Conclusions

In this study, we designed and characterized an extensive array of PS-MME CANs, prepared both in solution and in bulk from readily available polymers and monomers. The study focused on structure-property relationships, where the dynamic properties of CANs can be attributed to factors such as crosslink density, the choice of building blocks, and the molar mass of the thermoplastic precursors. The materials demonstrated mechanical, thermal, and rheological properties suitable for practical applications.

Investigations into the relaxation behavior of PS-MME materials, derived from high molecular weight PS-*co*-MA precursors, revealed unprecedented experimental relaxation profiles with distinct regimes that are defined by critical timescales and discrete flow regimes. It was rationalized how in some cases a single parameter, such as relaxation time, becomes insufficient

to provide a comprehensive view of relaxation time distributions in entangled systems. We therefore proposed the use of a Continuous Relaxation Spectra (CRS) analysis. Zero shear viscosity assessments, revealing up to two distinct viscoelastic flow regimes in entangled PS-MMEs, highlighted how thermally induced covalent bond exchanges are not the sole factor governing viscosity evolution in CANs. Overall, these findings underscored the intricate relationship between network connectivity, relaxation dynamics, and processability in dissociative dynamic polymer networks.

Moreover, high temperature FTIR and looped rheological analyses demonstrated the origin of the loss of dynamic properties previously observed in monoester-based dissociative CANs at temperatures above 170°C. While a tentative mechanism for thermal degradation of MME CANs, such as the formation of non-dynamic diesters via linear anhydride intermediates, has been proposed, we experimentally demonstrated that such reaction pathways are strongly hindered in PS-MME CANs up to at least 250°C. Thanks to this unprecedented thermal resilience, our materials can achieve flow rates that allow for continuous reprocessing *via* extrusion or injection molding, without degradation or property loss. Finally, leveraging the same dynamic equilibrium, the crosslinked materials could also be chemically recycled by shifting the equilibrium back to linear polymers and monomers through dilution and heating in an inert solvent.

Declaration of Competing Interest

The authors declare that they have no known competing monetary interests or personal relationships that could have appeared to influence the work reported in this paper.

Acknowledgements

This project has received funding from the European Union's Horizon 2020 research and innovation program under the Marie Skłodowska-Curie Grant agreement No 860911. The authors thank Bernhard De Meyer and Jan Goeman for technical support, Croda and Polyscope for kindly providing samples that were used in this project. Likewise, the authors express gratitude to Prof. Dr. Ludwig Cardon and Mustafa Erkoç for their logistic support and assistance during the extrusion experiments as well as Dr. Jérémy Odent and Prof. Dr. Jean-Marie Raquez for their assistance during the injection molding tests. Lastly, we acknowledge Dr. Chiel Mertens and Stephan Maes for the fruitful discussions held during the duration of this study.

Associated Content

Supplementary data to this article can be found as a Supporting Information file accessible free of charge *via* the Internet at "***to be provided***". The raw and processed data required to reproduce these findings are available upon request to the corresponding author.

References

(1) Shenoy, A.; Saini, D. *Thermoplastic Melt Rheology and Processing*; 1996.
(2) *Revolutionizing Aircraft Materials and Processes*; Pantelakis, S., Tserpes, K., Eds.; Springer International Publishing: Cham, 2020. https://doi.org/10.1007/978-3-030-35346-9.
(3) Toozandehjani, M. Conventional and Advanced Composites in Aerospace Industry: Technologies Revisited. *AJAE* **2018**, *5* (1), 9. https://doi.org/10.11648/j.ajae.20180501.12.
(4) Post, W.; Susa, A.; Blaauw, R.; Molenveld, K.; Knoop, R. J. I. A Review on the Potential and Limitations of Recyclable Thermosets for Structural Applications. *Polymer Reviews* **2020**, *60* (2), 359–388. https://doi.org/10.1080/15583724.2019.1673406.
(5) Montarnal, D.; Capelot, M.; Tournilhac, F.; Leibler, L. Silica-Like Malleable Materials from Permanent Organic Networks. *Science* **2011**, *334* (6058), 965–968. https://doi.org/10.1126/science.1212648.
(6) Bowman, C. N.; Kloxin, C. J. Covalent Adaptable Networks: Reversible Bond Structures Incorporated in Polymer Networks. *Angew. Chem. Int. Ed.* **2012**, *51* (18), 4272–4274. https://doi.org/10.1002/anie.201200708.
(7) Denissen, W.; Winne, J. M.; Du Prez, F. E. Vitrimers: Permanent Organic Networks with Glass-like Fluidity. *Chem. Sci.* **2016**, *7* (1), 30–38. https://doi.org/10.1039/C5SC02223A.
(8) Zhang, V.; Kang, B.; Accardo, J. V.; Kalow, J. A. Structure–Reactivity–Property Relationships in Covalent Adaptable Networks. *J. Am. Chem. Soc.* **2022**, jacs.2c08104. https://doi.org/10.1021/jacs.2c08104.

(9) Röttger, M.; Domenech, T.; van der Weegen, R.; Breuillac, A.; Nicolaÿ, R.; Leibler, L. High-Performance Vitrimers from Commodity Thermoplastics through Dioxaborolane Metathesis. *Science* **2017**, *356* (6333), 62–65. https://doi.org/10.1126/science.aah5281.
(10) Guerre, M.; Taplan, C.; Winne, J. M.; Du Prez, F. E. Vitrimers: Directing Chemical Reactivity to Control Material Properties. *Chem. Sci.* **2020**, *11* (19), 4855–4870. https://doi.org/10.1039/D0SC01069C.
(11) Altuna, F. I.; Casado, U.; dell'Erba, I. E.; Luna, L.; Hoppe, C. E.; Williams, R. J. J. Epoxy Vitrimers Incorporating Physical Crosslinks Produced by Self-Association of Alkyl Chains. *Polym. Chem.* **2020**, *11* (7), 1337–1347. https://doi.org/10.1039/C9PY01787A.
(12) Fan, M.; Liu, J.; Li, X.; Zhang, J.; Cheng, J. Recyclable Diels–Alder Furan/Maleimide Polymer Networks with Shape Memory Effect. *Ind. Eng. Chem. Res.* **2014**, *53* (42), 16156–16163. https://doi.org/10.1021/ie5028183.
(13) Winne, J. M.; Leibler, L.; Du Prez, F. E. Dynamic Covalent Chemistry in Polymer Networks: A Mechanistic Perspective. *Polym. Chem.* **2019**, *10* (45), 6091–6108. https://doi.org/10.1039/C9PY01260E.
(14) Jourdain, A.; Asbai, R.; Anaya, O.; Chehimi, M. M.; Drockenmuller, E.; Montarnal, D. Rheological Properties of Covalent Adaptable Networks with 1,2,3-Triazolium Cross-Links: The Missing Link between Vitrimers and Dissociative Networks. *Macromolecules* **2020**, *53* (6), 1884–1900. https://doi.org/10.1021/acs.macromol.9b02204.
(15) Elling, B. R.; Dichtel, W. R. Reprocessable Cross-Linked Polymer Networks: Are Associative Exchange Mechanisms Desirable? *ACS Cent. Sci.* **2020**, *6* (9), 1488–1496. https://doi.org/10.1021/acscentsci.0c00567.
(16) Bin Rusayyis, M. A.; Torkelson, J. M. Reprocessable Covalent Adaptable Networks with Excellent Elevated-Temperature Creep Resistance: Facilitation by Dynamic, Dissociative Bis(Hindered Amino) Disulfide Bonds. *Polym. Chem.* **2021**, *12* (18), 2760–2771. https://doi.org/10.1039/D1PY00187F.
(17) Podgórski, M.; Spurgin, N.; Mavila, S.; Bowman, C. N. Mixed Mechanisms of Bond Exchange in Covalent Adaptable Networks: Monitoring the Contribution of Reversible Exchange and Reversible Addition in Thiol–Succinic Anhydride Dynamic Networks. *Polym. Chem.* **2020**, *11* (33), 5365–5376. https://doi.org/10.1039/D0PY00091D.
(18) Podgórski, M.; Huang, S.; Bowman, C. N. Additive Manufacture of Dynamic Thiol–Ene Networks Incorporating Anhydride-Derived Reversible Thioester Links. *ACS Appl. Mater. Interfaces* **2021**, *13* (11), 12789–12796. https://doi.org/10.1021/acsami.0c18979.
(19) Delahaye, M.; Winne, J. M.; Du Prez, F. E. Internal Catalysis in Covalent Adaptable Networks: Phthalate Monoester Transesterification As a Versatile Dynamic Cross-Linking Chemistry. *J. Am. Chem. Soc.* **2019**, *141* (38), 15277–15287. https://doi.org/10.1021/jacs.9b07269.
(20) Adzima, B. J.; Aguirre, H. A.; Kloxin, C. J.; Scott, T. F.; Bowman, C. N. Rheological and Chemical Analysis of Reverse Gelation in a Covalently Cross-Linked Diels−Alder Polymer Network. *Macromolecules* **2008**, *41* (23), 9112–9117. https://doi.org/10.1021/ma801863d.
(21) Nakamura, Y.; Tenjimbayashi, M.; Moriya, A.; Naito, M. Impact of Telechelic Polymer Precursors on the Viscoelastic Properties of Vitrimers. *Macromolecular Chemistry and Physics* **2022**, *223* (7), 2100433. https://doi.org/10.1002/macp.202100433.
(22) Anaya, O.; Jourdain, A.; Antoniuk, I.; Ben Romdhane, H.; Montarnal, D.; Drockenmuller, E. Tuning the Viscosity Profiles of High- T_g Poly(1,2,3-Triazolium) Covalent Adaptable Networks by the Chemical Structure of the N-Substituents. *Macromolecules* **2021**, *54* (7), 3281–3292. https://doi.org/10.1021/acs.macromol.0c02221.
(23) Snyder, R. L.; Lidston, C. A. L.; De Hoe, G. X.; Parvulescu, M. J. S.; Hillmyer, M. A.; Coates, G. W. Mechanically Robust and Reprocessable Imine Exchange Networks from Modular Polyester Pre-Polymers. *Polym. Chem.* **2020**, *11* (33), 5346–5355. https://doi.org/10.1039/C9PY01957J.
(24) Leibler, L.; Rubinstein, M.; Colby, R. H. Dynamics of Reversible Networks. *Macromolecules* **1991**, *24* (16), 4701–4707. https://doi.org/10.1021/ma00016a034.

(25) Kar, G. P.; Saed, M. O.; Terentjev, E. M. Scalable Upcycling of Thermoplastic Polyolefins into Vitrimers through Transesterification. *J. Mater. Chem. A* **2020**, *8* (45), 24137–24147. https://doi.org/10.1039/D0TA07339C.
(26) Fenimore, L. M.; Chen, B.; Torkelson, J. M. Simple Upcycling of Virgin and Waste Polyethylene into Covalent Adaptable Networks: Catalyst-Free, Radical-Based Reactive Processing with Dialkylamino Disulfide Bonds. *J. Mater. Chem. A* **2022**, 10.1039.D2TA06364F. https://doi.org/10.1039/D2TA06364F.
(27) Ahmadi, M.; Hanifpour, A.; Ghiassinejad, S.; van Ruymbeke, E. Polyolefins Vitrimers: Design Principles and Applications. *Chem. Mater.* **2022**, acs.chemmater.2c02853. https://doi.org/10.1021/acs.chemmater.2c02853.
(28) Lossada, F.; Jiao, D.; Yao, X.; Walther, A. Waterborne Methacrylate-Based Vitrimers. *ACS Macro Lett.* **2020**, *9* (1), 70–76. https://doi.org/10.1021/acsmacrolett.9b00997.
(29) Santefort, A. L.; Yuya, P. A.; Shipp, D. A. Dynamic Covalent Exchange Induced Cyclization in Poly(Methacrylic Anhydride). *Polym. Chem.* **2022**, *13* (31), 4502–4510. https://doi.org/10.1039/D2PY00488G.
(30) Lessard, J. J.; Scheutz, G. M.; Hughes, R. W.; Sumerlin, B. S. Polystyrene-Based Vitrimers: Inexpensive and Recyclable Thermosets. *ACS Appl. Polym. Mater.* **2020**, *2* (8), 3044–3048. https://doi.org/10.1021/acsapm.0c00523.
(31) Lu, N.; Li, Q.; Ma, S.; Wang, B.; Xu, X.; Wang, S.; Ye, J.; Qiu, J.; Zhu, J. Scalable and Facile Synthesis of Acetal Covalent Adaptable Networks with Readily Adjustable Properties. *European Polymer Journal* **2021**, *147*, 110291. https://doi.org/10.1016/j.eurpolymj.2021.110291.
(32) Jia, Y.; Delaittre, G.; Tsotsalas, M. Covalent Adaptable Networks Based on Dynamic Alkoxyamine Bonds. *Macromolecular Materials and Engineering* **2022**, *307* (9), 2200178. https://doi.org/10.1002/mame.202200178.
(33) Van Lijsebetten, F.; Holloway, J. O.; Winne, J. M.; Du Prez, F. E. Internal Catalysis for Dynamic Covalent Chemistry Applications and Polymer Science. *Chem. Soc. Rev.* **2020**, *49* (23), 8425–8438. https://doi.org/10.1039/D0CS00452A.
(34) Delahaye, M.; Tanini, F.; Holloway, J. O.; Winne, J. M.; Du Prez, F. E. Double Neighbouring Group Participation for Ultrafast Exchange in Phthalate Monoester Networks. *Polym. Chem.* **2020**, *11* (32), 5207–5215. https://doi.org/10.1039/D0PY00681E.
(35) Zhang, H.; Majumdar, S.; van Benthem, R. A. T. M.; Sijbesma, R. P.; Heuts, J. P. A. Intramolecularly Catalyzed Dynamic Polyester Networks Using Neighboring Carboxylic and Sulfonic Acid Groups. *ACS Macro Lett.* **2020**, *9* (2), 272–277. https://doi.org/10.1021/acsmacrolett.9b01023.
(36) Van Lijsebetten, F.; Spiesschaert, Y.; Winne, J. M.; Du Prez, F. E. Reprocessing of Covalent Adaptable Polyamide Networks through Internal Catalysis and Ring-Size Effects. *J. Am. Chem. Soc.* **2021**, *143* (38), 15834–15844. https://doi.org/10.1021/jacs.1c07360.
(37) Chen, Y.; Zhang, H.; Majumdar, S.; van Benthem, R. A. T. M.; Heuts, J. P. A.; Sijbesma, R. P. Dynamic Polyamide Networks via Amide–Imide Exchange. *Macromolecules* **2021**, *54* (20), 9703–9711. https://doi.org/10.1021/acs.macromol.1c01389.
(38) Li, R.; Yu, W.; Zhou, C. Phase Behavior and Its Viscoelastic Responses of Poly(Methyl Methacrylate) and Poly(Styrene-Co-Maleic Anhydride) Blend Systems. *Polym. Bull.* **2006**, *56* (4), 455–466. https://doi.org/10.1007/s00289-005-0499-6.
(39) Majumdar, B.; Keskkula, H.; Paul, D. R. Morphology of Nylon 6/ABS Blends Compatibilized by a Styrene/Maleic Anhydride Copolymer. *Polymer* **1994**, *35* (15), 3164–3172. https://doi.org/10.1016/0032-3861(94)90117-1.
(40) Bapat, A. P.; Ray, J. G.; Savin, D. A.; Hoff, E. A.; Patton, D. L.; Sumerlin, B. S. Dynamic-Covalent Nanostructures Prepared by Diels–Alder Reactions of Styrene-Maleic Anhydride-Derived Copolymers Obtained by One-Step Cascade Block Copolymerization. *Polym. Chem.* **2012**, *3* (11), 3112. https://doi.org/10.1039/c2py20351k.

(41) Saed, M. O.; Lin, X.; Terentjev, E. M. Dynamic Semicrystalline Networks of Polypropylene with Thiol-Anhydride Exchangeable Crosslinks. *ACS Appl. Mater. Interfaces* **2021**, *13* (35), 42044–42051. https://doi.org/10.1021/acsami.1c12099.
(42) Hu, K.; Wang, B.; Xu, X.; Su, Y.; Zhang, W.; Zhou, S.; Zhang, C.; Zhu, J.; Ma, S. Dual-Dynamic Chemistries-Based Fast-Reprocessing and High-Performance Covalent Adaptable Networks. *Macromolecular Rapid Communications*, 2200726. https://doi.org/10.1002/marc.202200726.
(43) Peterson, A.; Roy, M.; Fagerlund, J.; Re, G. L.; Müller, C. Synergistic Reinforcement of a Reversible Diels–Alder Type Network with Nanocellulose. *Materials Advances* **2021**, *2* (15), 5171–5180. https://doi.org/10.1039/D1MA00291K.
(44) Wang, S.; Ma, S.; Qiu, J.; Tian, A.; Li, Q.; Xu, X.; Wang, B.; Lu, N.; Liu, Y.; Zhu, J. Upcycling of Post-Consumer Polyolefin Plastics to Covalent Adaptable Networks *via in Situ* Continuous Extrusion Cross-Linking. *Green Chem.* **2021**, *23* (8), 2931–2937. https://doi.org/10.1039/D0GC04337K.
(45) Gao, Y.; Niu, H. Polypropylene-Based Transesterification Covalent Adaptable Networks with Internal Catalysis. *Polym. Chem.* **2024**, *15* (9), 884–895. https://doi.org/10.1039/D3PY01418E.
(46) Maiheu, T.; Debuyck, J.; Van Lijsebetten, F.; Hernández, A.; Du Prez, F. E. Polyisoprene-Based Pressure-Sensitive Adhesives with Dynamic Crosslinks. *European Polymer Journal* **2024**, *210*, 112998. https://doi.org/10.1016/j.eurpolymj.2024.112998.
(47) Meyersohn, M. S.; Haque, F. M.; Hillmyer, M. A. Dynamic Aliphatic Polyester Elastomers Crosslinked with Aliphatic Dianhydrides. *ACS Polym. Au* **2023**, acspolymersau.3c00004. https://doi.org/10.1021/acspolymersau.3c00004.
(48) Plazek, D. J.; O'Rourke, V. M. Viscoelastic Behavior of Low Molecular Weight Polystyrene. *J. Polym. Sci. A-2 Polym. Phys.* **1971**, *9* (2), 209–243. https://doi.org/10.1002/pol.1971.160090202.
(49) Singh, M. K.; Hu, M.; Cang, Y.; Hsu, H.-P.; Therien-Aubin, H.; Koynov, K.; Fytas, G.; Landfester, K.; Kremer, K. Glass Transition of Disentangled and Entangled Polymer Melts: Single-Chain-Nanoparticles Approach. *Macromolecules* **2020**, *53* (17), 7312–7321. https://doi.org/10.1021/acs.macromol.0c00550.
(50) Klumperman, B. Mechanistic Considerations on Styrene–Maleic Anhydride Copolymerization Reactions. *Polym. Chem.* **2010**, *1* (5), 558. https://doi.org/10.1039/b9py00341j.
(51) Klumperman, B.; Heuts, J. P. A. The Solution Copolymerization of Styrene and Maleic Anhydride in a Continuous Stirred Tank Reactor and Its Theoretical Modelling. *Polymer* **2020**, *202*, 122730. https://doi.org/10.1016/j.polymer.2020.122730.
(52) Mangialetto, J.; Cuvellier, A.; Verhelle, R.; Brancart, J.; Rahier, H.; Van Assche, G.; Van den Brande, N.; Van Mele, B. Diffusion- and Mobility-Controlled Self-Healing Polymer Networks with Dynamic Covalent Bonding. *Macromolecules* **2019**, *52* (21), 8440–8452. https://doi.org/10.1021/acs.macromol.9b01453.
(53) Van Lijsebetten, F.; De Bruycker, K.; Van Ruymbeke, E.; Winne, J. M.; Du Prez, F. E. Characterising Different Molecular Landscapes in Dynamic Covalent Networks. *Chem. Sci.* **2022**, *13* (43), 12865–12875. https://doi.org/10.1039/D2SC05528G.
(54) Palmlöf, M.; Hjertberg, T.; Sultan, B.-Å. Crosslinking Reactions of Ethylene Vinyl Silane Copolymers at Processing Temperatures. *J. Appl. Polym. Sci.* **1991**, *42* (5), 1193–1203. https://doi.org/10.1002/app.1991.070420504.
(55) *Recent insights into continuous-flow biodiesel production via catalytic and non-catalytic transesterification processes | Elsevier Enhanced Reader*. https://doi.org/10.1016/j.apenergy.2016.11.006.
(56) Prasanna Rani, K. N.; Ramana Neeharika, T. S. V.; Kumar, T. P.; Satyavathi, B.; Sailu, C. Kinetics of Non-Catalytic Esterification of Free Fatty Acids Present in Jatropha Oil. *J. Oleo Sci.* **2016**, *65* (5), 441–445. https://doi.org/10.5650/jos.ess15255.
(57) Delahaye, M. Recyclable Polymer Networks Based on Internally Catalysed Exchange Reactions. dissertation, Ghent University, 2020. http://hdl.handle.net/1854/LU-8655843 (accessed 2022-12-19).

(58) Maes, S.; Van Lijsebetten, F.; Winne, J. M.; Du Prez, F. E. *N* -Sulfonyl Urethanes to Design Polyurethane Networks with Temperature-Controlled Dynamicity. *Macromolecules* **2023**, *56* (5), 1934–1944. https://doi.org/10.1021/acs.macromol.2c02456.
(59) Watanabe, K. Stress Relaxation and Creep of Several Vulcanized Elastomers. *Rubber Chemistry and Technology* **1962**, *35* (1), 182–199. https://doi.org/10.5254/1.3539889.
(60) Münstedt, H. Rheological Experiments at Constant Stress as Efficient Method to Characterize Polymeric Materials. *Journal of Rheology* **2014**, *58* (3), 565–587. https://doi.org/10.1122/1.4866049.
(61) Hubbard, A. M.; Ren, Y.; Picu, C. R.; Sarvestani, A.; Konkolewicz, D.; Roy, A. K.; Varshney, V.; Nepal, D. Creep Mechanics of Epoxy Vitrimer Materials. *ACS Appl. Polym. Mater.* **2022**, *4* (6), 4254–4263. https://doi.org/10.1021/acsapm.2c00230.
(62) Porath, L. E.; Evans, C. M. Importance of Broad Temperature Windows and Multiple Rheological Approaches for Probing Viscoelasticity and Entropic Elasticity in Vitrimers. *Macromolecules* **2021**, *54* (10), 4782–4791. https://doi.org/10.1021/acs.macromol.0c02800.
(63) Martins, M. L.; Zhao, X.; Demchuk, Z.; Luo, J.; Carden, G. P.; Toleutay, G.; Sokolov, A. P. Viscoelasticity of Polymers with Dynamic Covalent Bonds: Concepts and Misconceptions. *Macromolecules* **2023**, *56* (21), 8688–8696. https://doi.org/10.1021/acs.macromol.3c01545.
(64) Shanbhag, S. pyReSpect: A Computer Program to Extract Discrete and Continuous Spectra from Stress Relaxation Experiments. *Macromolecular Theory and Simulations* **2019**, *28* (3), 1900005. https://doi.org/10.1002/mats.201900005.
(65) Porath, L.; Huang, J.; Ramlawi, N.; Derkaloustian, M.; Ewoldt, R. H.; Evans, C. M. Relaxation of Vitrimers with Kinetically Distinct Mixed Dynamic Bonds. *Macromolecules* **2022**, *55* (11), 4450–4458. https://doi.org/10.1021/acs.macromol.1c02613.
(66) Porath, L. E.; Ramlawi, N.; Huang, J.; Hossain, M. T.; Derkaloustian, M.; Ewoldt, R. H.; Evans, C. M. Molecular Design of Multimodal Viscoelastic Spectra Using Vitrimers. *Chem. Mater.* **2024**, *36* (4), 1966–1974. https://doi.org/10.1021/acs.chemmater.3c02852.
(67) Van Lijsebetten, F.; Debsharma, T.; Winne, J. M.; Du Prez, F. E. A Highly Dynamic Covalent Polymer Network without Creep: Mission Impossible? *Angewandte Chemie International Edition*, e202210405. https://doi.org/10.1002/anie.202210405.
(68) Lessard, J. J.; Stewart, K. A.; Sumerlin, B. S. Controlling Dynamics of Associative Networks through Primary Chain Length. *Macromolecules* **2022**, *55* (22), 10052–10061. https://doi.org/10.1021/acs.macromol.2c01909.
(69) Ricarte, R. G.; Shanbhag, S. Unentangled Vitrimer Melts: Interplay between Chain Relaxation and Cross-Link Exchange Controls Linear Rheology. *Macromolecules* **2021**, *54* (7), 3304–3320. https://doi.org/10.1021/acs.macromol.0c02530.
(70) Shao, J.; Jiang, N.; Zhang, H.; Yang, Y.; Tang, P. Sticky Rouse Model and Molecular Dynamics Simulation for Dual Polymer Networks. *Macromolecules* **2022**, *55* (2), 535–549. https://doi.org/10.1021/acs.macromol.1c02059.
(71) Cui, X.; Jiang, N.; Shao, J.; Zhang, H.; Yang, Y.; Tang, P. Linear and Nonlinear Viscoelasticities of Dissociative and Associative Covalent Adaptable Networks: Discrepancies and Limits. *Macromolecules* **2023**, *56* (3), 772–784. https://doi.org/10.1021/acs.macromol.2c02122.
(72) Xia, J.; Kalow, J. A.; Olvera de la Cruz, M. Structure, Dynamics, and Rheology of Vitrimers. *Macromolecules* **2023**, *56* (19), 8080–8093. https://doi.org/10.1021/acs.macromol.3c01366.
(73) Provencher, S. W. CONTIN: A General Purpose Constrained Regularization Program for Inverting Noisy Linear Algebraic and Integral Equations. *Computer Physics Communications* **1982**, *27* (3), 229–242. https://doi.org/10.1016/0010-4655(82)90174-6.
(74) Ricarte, R. G.; Shanbhag, S. A Tutorial Review of Linear Rheology for Polymer Chemists: Basics and Best Practices for Covalent Adaptable Networks. *Polym. Chem.* **2024**, *15* (9), 815–846. https://doi.org/10.1039/D3PY01367G.

(75) Mours, M.; Winter, H. H. Chapter 5 - Mechanical Spectroscopy of Polymers. In *Experimental Methods in Polymer Science*; Tanaka, T., Ed.; Polymers, Interfaces and Biomaterials; Academic Press: Boston, 2000; pp 495–546. https://doi.org/10.1016/B978-0-08-050612-8.50011-8.
(76) Zhu, L.; Xu, L.; Jie, S.; Li, B.-G. Preparation of Styrene–Butadiene Rubber Vitrimers with High Strength and Toughness through Imine and Hydrogen Bonds. *Ind. Eng. Chem. Res.* **2022**, acs.iecr.2c03133. https://doi.org/10.1021/acs.iecr.2c03133.
(77) Qin, B.; Liu, S.; Huang, Z.; Zeng, L.; Xu, J.-F.; Zhang, X. Closed-Loop Chemical Recycling of Cross-Linked Polymeric Materials Based on Reversible Amidation Chemistry. *Nat Commun* **2022**, *13* (1), 7595. https://doi.org/10.1038/s41467-022-35365-4.
(78) Lei, Z.; Chen, H.; Luo, C.; Rong, Y.; Hu, Y.; Jin, Y.; Long, R.; Yu, K.; Zhang, W. Recyclable and Malleable Thermosets Enabled by Activating Dormant Dynamic Linkages. *Nat. Chem.* **2022**. https://doi.org/10.1038/s41557-022-01046-4.
(79) Türel, T.; Tomović, Ž. Chemically Recyclable and Upcyclable Epoxy Resins Derived from Vanillin. *ACS Sustainable Chem. Eng.* **2023**, *11* (22), 8308–8316. https://doi.org/10.1021/acssuschemeng.3c00761.
(80) Ahrens, A.; Bonde, A.; Sun, H.; Wittig, N. K.; Hammershøj, H. C. D.; Batista, G. M. F.; Sommerfeldt, A.; Frølich, S.; Birkedal, H.; Skrydstrup, T. Catalytic Disconnection of C–O Bonds in Epoxy Resins and Composites. *Nature* **2023**, *617* (7962), 730–737. https://doi.org/10.1038/s41586-023-05944-6.

TOC Synopsis: From commercially available poly(styrene-*co*-maleic anhydride) and diols, fully transparent and (re)processable maleate-monoester containing polystyrene-inspired covalent adaptable networks were obtained and analyzed. These materials could then be reprocessed via injection molding and single screw continuous extrusion. Lastly, the feasibility for the regeneration and separation of the initial building blocks and the regeneration of the original network was demonstrated as chemical recycling strategies.

Table of Contents: